TECHNISCHE
UNIVERSITÄT
WIEN

Diplomarbeit

Electron-stimulated Desorption of Lunar Surface Regolith Analogues

ausgeführt am Institut für Angewandte Physik
der Technischen Universität Wien
Wiedner Hauptstraße 8-10/E134
1040 Wien

unter der Anleitung von
Univ.-Prof. Dr. Friedrich Aumayr
Dipl.-Ing. Johannes Brötzner, BSc

durch

Fuchs Lea, BSc
Matrikelnummer 11778931

8. Mai 2024

Unterschrift Betreuer

Unterschrift StudentIn

Abstract

Electrons within the solar wind can interact with surfaces of rocky bodies without a magnetic field or atmosphere. The composition of the exosphere is linked to surface properties like its composition, which presents an opportunity to gather surface information through exosphere analysis during flyby missions. Although data regarding the impact of ions from the solar wind on exosphere formation are available, information on the influence of electrons, especially regarding mass loss due to electron stimulated desorption (ESD) processes, is relatively limited.

In this thesis, the mass removal caused by ESD on the lunar analogue material enstatite is investigated. For this purpose, the quartz crystal microbalance (QCM) technique is used. Thereby, a thin film of the analoge material is deposited on one gold electrode of a quartz resonator, and by observing changes in the resonance frequency, information about mass changes is gained in real time and *in situ*. After developing an experimental protocol to use the QCM implemented at the Institute of Applied Physics at TU Wien also for electron-stimulated desorption measurements, the electron beam emitted by the *FS40A1* electron source from *PREVAC* is analyzed.

With the electron beam, measurement regarding the desorption of particles from the lunar analogue material enstatite $MgSiO_3$ under electron irradiation with electron energies in the range of $10\,\mathrm{eV} - 500\,\mathrm{eV}$ were carried out. A threshold energy for desorption was found and a linear correlation between electron energy and the mass ejection was observed. Additional experiments with LiF, a sample material with a well-documented high desorption yield, also demonstrated a linear correlation between electron impact energy and desorbed mass at a sample temperature of 120°C. At room temperature, this linear correlation could not be observed. A possible explanation could be charging of the sample under electron irradiation, but further measurements will be needed to confirm this hypotheses.

Kurzfassung

Elektronen innerhalb des Sonnenwinds können ungehindert mit Oberflächen von Gesteinskörpern in Abwesenheit eines Magnetfelds oder einer Atmosphäre interagieren. Die Zusammensetzung der Exosphäre basiert auf der Oberflächenbeschaffenheit, was die Möglichkeit bietet, Informationen bezüglich der Oberfläche durch Exosphärenanalyse während Flyby-Missionen zu sammeln. Obwohl Daten über den Einfluss von Ionen aus dem Sonnenwind auf die Exosphärenbildung vorliegen, sind die Informationen zum Einfluss der Elektronen bisher relativ begrenzt.

In dieser Arbeit wird der Massenabtrag durch elektronenstimulierte Desorption an lunarem Analogmaterial Enstatit untersucht. Zu diesem Zweck wurde die Quarzkristallmikrowaage (QCM) Technik verwendet. In diesem Fall wird eine dünne Schicht des zu untersuchenden Materials auf einen gold Quarz aufgebracht und bei Beobachtung der Veränderung der Resonanzfrequenz des Quarzes, können Informationen über Massenveränderungen in Echtzeit und in situ erhalten werden.

Nachdem ein Verfahren zur Messung der durch Elektronenstimulation ausgelösten Desorption entwickelt wurde, wurde der von der Elektronenquelle *FS40A1* von *PREVAC* emittierte Elektronenstrahl analysiert.

Mit dem Elektronenstrahl wurden Messungen zur Desorption von Teilchen aus dem lunaren Analogmaterial Enstatit $MgSiO_3$ unter Elektronenbestrahlung mit Elektronenenergien im Bereich von $10\,\text{eV} - 500\,\text{eV}$ durchgeführt. Dabei wurde eine Schwellenenergie bestimmt und eine lineare Korrelation zwischen Elektronenenergie und dem Massenabtrag beobachtet.

Zusätzliche Experimente mit LiF, einem Probenmaterial mit gut dokumentierten hohen Desorptionseffekten, zeigten ebenfalls eine lineare Korrelation zwischen Energie und Masseneliminierung bei einer Temperatur von 120°C. Bei Raumtemperatur konnte dieser lineare Zusammenhang nicht festgestellt werden. Eine mögliche Erklärung könnte die Aufladung der Probe unter Bestrahlung mit Elektronen sein aber weitere Messungen wären notwendig um diese Hypothese zu bestätigen.

Contents

1 Introduction

1.1 Motivation

Space's challenging environment exerts a substantial impact, particularly on airless bodies, affecting their surfaces. These prevailing conditions lead to changes in both the surface structure and composition of planetary bodies.

The term *space weathering* is used to summarize the effects of micrometeoroid impacts [1], electromagnetic irradiation [2], and the bombardment of ions and electrons from the solar wind, among others [3]. On the Moon, these effects are visible both through the formation of craters [4] due to meteorite impact [5] and through a darkened crust and an amorphized rim on the surface grains argued to be caused by sputtering processes through ions of the solar wind [6].

Besides alteration of chemical and optical surface properties, these processes also eject material from the rocky bodies, resulting in the formation of a tenuous gas layer, the exosphere. In this case the ejected particles follow ballistic trajectories back to the surface unless their energies exceed the escape velocity of the corresponding object and they leave the gravitational field [7]. The composition of the exosphere is therefore linked to the underlying surface [8]. Examining the exosphere offers a means to gain a deeper understanding of the composition and characteristics of the surface. Exospheric data can be collected during flyby operations [9]. These maneuvers mark a substantial advance compared to the intricate and error-prone direct surface landings. A recent illustration of these challenges is evident in the failed attempt of the Russian lunar lander *Luna-25* to successfully land on the lunar surface [10].

Moreover, successful flyby maneuvers have already been executed, for example, the *MESSENGER* spacecraft orbiting Mercury, and the ongoing *Artemis* missions [9]. Besides aiming to bring humans back to the Moon, also in-situ data on the lunar exosphere are collected during the *Artemis* missions [11]. Also in previous missions the composition of the lunar surface and the lunar exosphere were examined more precisely. For example, the elements helium (He), argon (Ar), sodium (Na) and potassium (K) were detected as constituents of the exosphere [12, 13]. Diverse mechanisms including impact of solar wind constituants cause the release of these elements [14].

The solar wind constitutes a continuous flux of charged particles emanating from the Sun's outermost layer, the so-called corona [15]. This solar wind can be classified into two categories: The fast solar wind typically reaches a velocity of about 750 km/s and maintains a temperature in the vicinity of 800 MK [16, 17]. Its elemental composition closely parallels that of the Sun's photosphere. The slow solar wind, on the other hand, has typical velocities ranging from 300 to 500 km/s, while maintaining a temperature of approximately 100 MK [18]. The solar wind consists primarily of protons, alpha particles and electrons. When considering electrons in the solar wind, they can be classified into four distinct categories based on their energy levels [7]. The majority of the electrons are assigned to the so-called *core* with an energy of less than 60 eV. Followed by an isotropic supra-thermal population called *halo* with energies between 60 eV and 1 keV. The *Strahl* population typically exhibits energies in the range of several hundred electron volts and demonstrates strong alignment with the magnetic field of the Sun and the *super halo* extends beyond 1 keV [19, 7, 20].

In the recent past, the influence of solar wind ion irradiation on relevant minerals has been extensively studied [21, 22, 23, 24]. Additionally, the effects of photons and electrons are gaining prominence in research inquiries [25]. Summarized by the terms desorption by electronic transitions (DIET) [26], electron-stimulated desorption (ESD) and photon-stimulated desorption (PSD), these effects [27] can also lead to the ejection of surface particles. While ESD has demonstrated its relevance when it comes to changes in the surface composition [28], the influence of electrons on the lunar surface remains an interesting and developing research area.

In recent years, the Quartz Crystal Microbalance (QCM) [29] technique utilized at TU Wien has played a significant role in the understanding of ion sputtering [30, 31]. This technique should now also be used to resolve a possible mass change during electron bombardment. For this purpose, enstatite $MgSiO_3$ was chosen as a sample, as it serves as an analog material for both the Moon and Mercury, and its behavior under ion bombardment is already known [22, 31]. Furthermore, the sample was already available and no time delay in course of the measurements occurred.

1.2 Electron-Stimulated Desorption (ESD)

When electrons with typical energies ranging from 10 eV to 1000 eV interact with solid surfaces which are covered with adsorbate layers, changes in the surface composition can occur. The bound states between the adsorbates and the solid surface can be electronically excited, leading to the release of neutrals and ions from the adsorbate. Due to the substantial mass difference between the impacting electrons and the emitted particles, electronic excitation must be considered instead of kinetic sputtering. This release of particles due to electron bombardment and the resulting electronic excitation is further called electron-stimulated desorption (ESD). The desorption of particles due to ESD was first explained by Menzel, Gomer and Redhead via a Franck-Condon transition and is further described in the Menzel-Gomer-Redhead (MGR) model [32, 33].

1.2.1 Franck-Condon transition and MGR Model

When an adsorbate is applied to a substrate surface, the potential energy function of molecules of the adsorbate in the ground and excited electronic states is described by the Morse-like potential [34], as illustrated in Figure 1.1. At equilibrium, a molecule will be in the nuclear configuration corresponding to the minimum potential energy, i.e., at the positions z_0 for the ground state E_0 and z_1 for the excited state E_1, respectively [35]. The z-axis represents the distance between the adsorbate molecule and the underlying substrate surface.

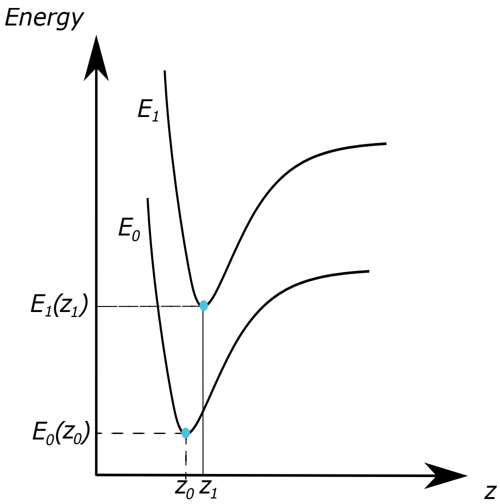

Figure 1.1: Potential energy function of the ground and excited electronic states.The z-axis represents the distance between the adsorbate molecule and the underlying substrate surface. At equilibrium, the potential energies are minimized at z_0 and z_1 with the corresponding energies E_0 and E_1, respectively. Figure adapted from [28]

When an electron interacts with the adsorbate-surface-system, the electronic energy state of a molecule in the adsorbate can change. This transition is called the Franck-Condon transition, and because of the small electron mass, the transition takes place instantaneously [36]. In the graphical illustration, this transition is represented by a vertical arrow (compare Figure 1.2) and is therefore also called a vertical transition. The probability of this process depends on the electronic and vibrational state of the involved molecule.

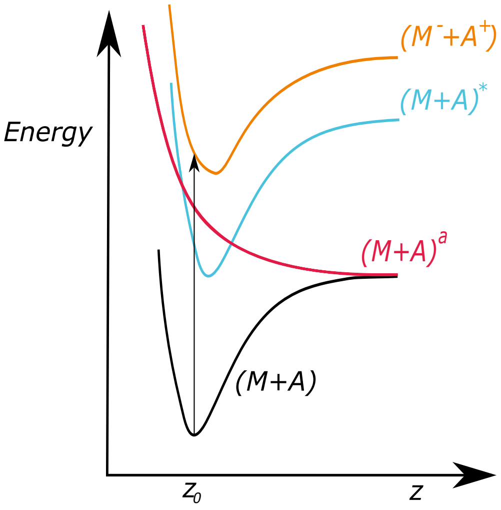

Figure 1.2: Potential energy curves for a ground state $(M + A)$ of an adsorbate(A)-substrate(M) system and different excited states $(M + A)^a$ described by an anti-bonding state, $(M + A)^*$ a metastable and $(M^- + A^+)$ an ionic state. Figure adapted from [28]

Such a Franck-Condon transition can occur from the same ground state $M + A$ of an adsorbate(A)-substrate(M) system to different excited states. Figure 1.2 also illustrates different potential curves for an anti-bonding state $(M + A)^a$, a metastable state $(M + A)^*$, and an ionic state $(M^- + A^+)$. However, a Franck-Condon transition does not necessarily lead to the ejection of a particle. For desorption to occur, another condition must also be fulfilled [37], summarized in the Menzel-Gomer-Redhead (MGR) model. The interaction of electrons with the surface in the quantum mechanical picture is described by the MGR model.

To release a particle to an anti-bonding state, its kinetic energy E_K must overcome the recapture barrier E_R, as illustrated in Figure 1.3. Otherwise, the particle will be recaptured in the ground state. In this case the energies E_K and E_R represent the energy liberated during the transition to either the excited or ground state. This condition is fulfilled at a certain position z_c. If the distance between the adsorbate molecule and the underlying substrate surface is smaller than z_c, for example the position z_G, the corresponding energies E_T and E_G to the excited state and the ground state are shifted. Since the energy difference $E_T < E_G$, it is more energetically favorable for the particle to return to the ground state. Thus, it can be generalized that if $z < z_c$, the particle will be recaptured in the ground state [28].

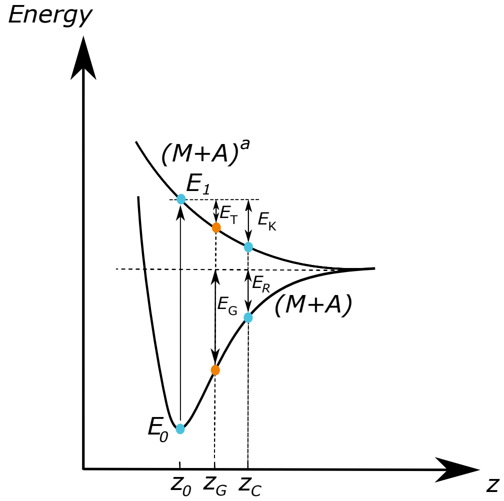

Figure 1.3: Threshold value E_R for the kinetic energy E_K as to be overcome for the release of a particle. Otherwise its recaptured in the ground state, illustrated with the energies E_T and E_G. The fulfillment of $z > z_c$ is also a possible way to formulate the requirement for the release of a particle according to the MGR model. Figure adapted from [28]

The specific thresholds for ESD processes depend on the kinetic energy E_k values, which in turn depend on the shape and relative positions of the ground and excited states [37].

1.2.2 The Knotek-Feibelman (KF) Model for Desorption

When investigating ionic maximal valency oxide surfaces, such as TiO_2, it was discovered that electron energies below 20 eV resulted in a small total desorption yield. This contradicts the expectations of the MGR model, which predicts high desorption of neutral particles. When the electron energy was increased to 25-35 eV, the desorption of the anion component was detected as positive ions. Knotek and Feibelman therefore established a model for desorption (KF model) which tries to explain the desorption of the anion component as a positive ion and the small ESD yields for oxide surfaces for incident electron energies under 20 eV [38]. In maximal valency ionic compound such as TiO_2, the cation is ionized up to the noble gas configuration. In this case, this corresponds to Ti^{4+}. In this configuration, the oxygen is bound in a O^{2-} state, however when it comes to desorption, positive ions are detected. This implies that charge transfer occurred during the desorption process. Figure 1.4 illustrates a simplified schematic of the process that leads to the desorption of O^+ from an initial ground state surface configuration of $Ti^{4+}O_2^{2-}$ [34].

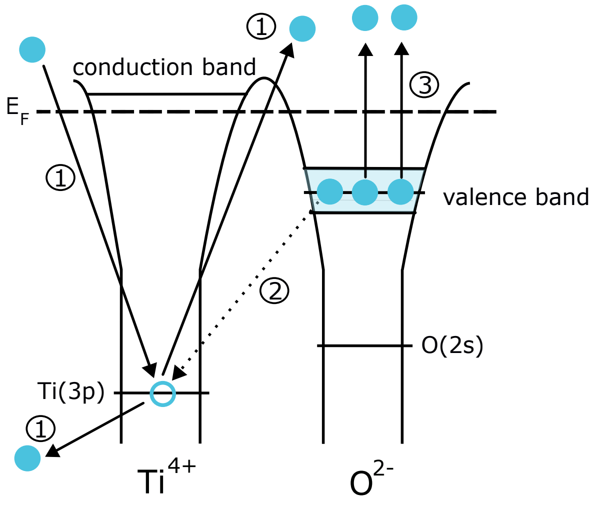

Figure 1.4: KF model for desorption of maximal valency ionic compound using the example of TiO_2. The created hole in the 3p level of the Ti due to electron bombardment (1) is filled via an inter-atomic Auger-Meitner process with an electron from the O^{-2} ion (2). By the released energy, two electrons from the oxygen are ejected (3). The created O^+ ion is emitted through Coulomb repulsion. Figure adapted from [37]

When an electron is ejected from the 3p level of the Ti, which is located approxi-

mately 35 eV below the conduction band minimum, during electron bombardment (1), the created hole would normally be filled by an intra-atomic Auger-Meitner process from a higher lying Ti level. Since in a maximal valency ionic compound the cation is in a Ti^{4+} state, no valence electrons are available. Therefore, the created hole is filled by an intra-atomic Auger-Meitner process with an electron from the O^{2-} ion (process 2 in Figure 1.4). Furthermore, two electrons from the oxygen will be ejected to release the energy of the decay (3), which leaves the oxygen in an O^{+} state. Coulomb repulsion with the surrounding positiv charged Ti ions leads to the emission of O^{+}.
With this model, the large charge transfer during the desorption as well as the energy threshold of desorption of oxygen ions of 35 eV are explained: The threshold corresponds to the ionization energy of Ti(3 p), which is the first process in the cascade leading to the desorption of O^{+}.

The KF-model can also be illustrated using lithium fluoride (LiF). LiF is an alkali halide that is known to exhibit ESD and therefore served as a control sample during the course of this thesis [39]. However, while the desorption of Li^{+} and F^{+} can be explained using the KF-model, while also neutral F^{0} and Li^{0} were experimentally observed [40]. In this case the so-called defect-mediated desorption mechanism needs to be taken into account.

1.2.3 Defect-mediated Desorption

In this model, the desorption of neutral particles can be explained by formation of localized defects, e.g. self-trapped excitons (STE) or self-trapped holes (STH), in the material as response to an electronic excitation [41, 40]. The model is illustrated in Figure 1.5 using LiF as an example, which is a large band gap insulator with a band gap of $W_\phi = 14\,\mathrm{eV}$ [42]. Electron bombardment causes an electron from the 2p level of the fluorine to be excited into the valence band, resulting in the formation of an electron-hole pair, as shown in Figure 1.5a.

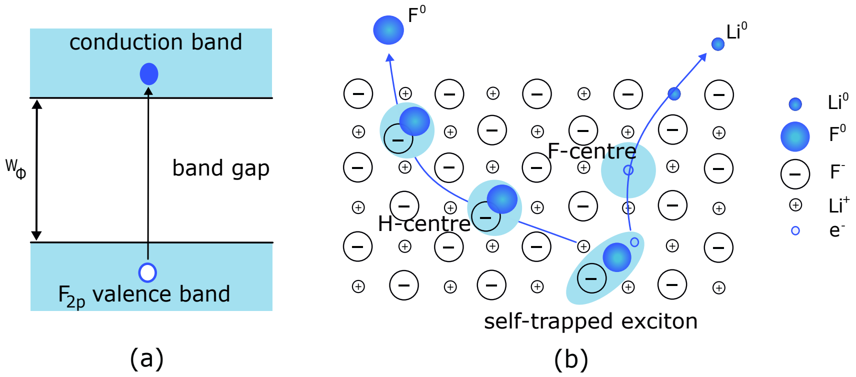

Figure 1.5: Electronic excitation of LiF under electron bombardment (a) and formation of localized defects (b). The defects, in this case STE, further decay into color centers leading to the desorption of F^0 and Li^0. Figure adapted from [41]

In alkali halides, energy is efficiently transferred from the electronic system to the phononic system due to the strong electron-phonon coupling. This process leads to the creation of localized defects, such as self-trapped holes and self-trapped excitons [43, 44]. In the case of LiF, illustrated in Figure 1.5b, the self-trapped exciton is composed of a F^0, an electron and a F^- neighbor [43]. Further, the STEs or STHs decay into different color centers: In the case of LiF, these are H- and F-centres [45]. The H-center consists of an ${F_2}^-$ molecular ion and is located at one anion lattice site while the F-center, in this case an electron, is situated at the next or second-next anion site. The different color centers can migrate to the surface and in this context desorption occurs. The F-center electron neutralizes an Li^+ cation and the H-center emits an F^0 atom. If not desorbed the created neutral Li atoms form a metallic overlayer on the surface and thereby the emission of particles at room temperature due to electron bombardment is suppressed. However, by increasing the surface temperature up to 150°C, the metallic layer can evaporate [41].

Additionally, it should be highlighted that metals exhibit such high conductivity that the electrons are rapidly transported throughout the lattice, thereby preventing the formation of localized defects. The phenomenon of defect-mediated sputtering is also observed during potential sputtering, suggesting a similar response for identical target samples upon irradiation with highly charged ions [41].

1.3 State of the Art and Aim of the Thesis

Since the first theory concerning ESD was proposed by Menzel, Gomer and Redhead in 1964 [36, 33], a variety of different models have been developed [37]. Especially in combination with fluorine, various studies on ESD processes have been conducted. Often thin films of lithium fluoride have been used in combination with an electron beam at energies of up to some hundred eV. The effects of electron interaction were further investigated by analyzing surface changes [46] or by detecting desorbed particles [47].

An energy threshold for ESD has been detected with respect to LiF films [48]. This implies that the sample must be exposed to electrons with an energy of minimum 10 eV - 30 eV before desorption of Li^+ or F^+ ions can be detected. Furthermore, the threshold of F^+ ions is lower and therefore more than one F^+ ion has to be ejected in order to emit a Li^+ ion. This further leads to an enrichment (3:1) of lithium in the surface region [46].

In addition to this topic, electrons and ESD processes are becoming more and more interesting in the space weathering and solar system sciences context [25]. As part of the solar wind, electrons interact with celestial objects and might contribute to the formation of a surrounding exosphere on rocky bodies such as the Moon or Mercury. Regarding the lunar exosphere, precise measurements of Na and K concentrations were conducted as described in [13]. In this context, electron bombardment was examined to lead to the ejection of ions Na and K that are therefore present in the exosphere composition of the Moon and Mercury.

Already in the study by Yakshinskiy *et al.* from the year 1999, the desorption of priorly adsorbed Na of a SiO_2 film under electron bombardment was observed [49]. In this case electron energies up to 40 eV have been used and an energy threshold for electron-stimulated desorption has been found. The desorption of Na from a lunar sample was later investigated in [27]. Here, also a temperature dependence of the measured ESD cross section was determined. Further, the results for the desorption of Na from the lunar sample and the SiO_2 bulk were compared in [50, 51]. In general, the desorption of alkali atoms and ions from oxide surfaces was investigated in [52]. Thereby, besides electron-stimulated desorption also thermal and photon-stimulated desorption were taken into account. All of these experiments focus on the desorption mostly of alkali species from different substrates like lunar samples or quartz. These samples were however evaporated onto the subtrastes immediately before the experiments, while any desorption from mineral substrate as a potential material property has hardly been analyzed. Moreover, the importance of ESD has not yet been fully clarified. While some studies emphasize the significance of

ESD on the erosion of the surface on rocky bodies [25], others point to a potential overestimation of its influence [53]. This thesis aims to shed light on this issue by investigating potential ESD from enstatite ($MgSiO_3$) as a proxy for the pyroxene contribution to the lunar or hermean mineralogy using the QCM technique. The QCM technique was previously employed at TU Wien to study mass removal due to ion incidence. Now, a similar approach will be adapted to measure mass changes resulting from electron bombardment. Certain modifications to the current workflow are necessary to perform these experiments. The effectiveness of these adjustments will subsequently be verified using different samples with known behavior upon electron impact.

2 Experimental Methods and Setup

In this section, the Quartz Crystal Microbalance (QCM) technique employed in the experiments is described, followed by a more in-depth explanation of the *AUGUSTIN* ion beam facility at the Institute of Applied Physics (IAP) at TU Wien and its ECR ion source known as *SOPHIE*. Subsequently, the experimental chamber at the end of Beam Line 3 (*BL3*) is explained. In conclusion, details regarding the utilized electron flood gun *FS40A1* electron source are presented.

2.1 Sputtering

The term sputtering describes the removal of particles by ion bombardment at energies of a few eV to several MeV [54, 55]. Also for sputtering processes there is a threshold which has to be overcome in order to eject a particle from the surface. In more precise terms, the particle's surface binding energy must be lower than the portion of the kinetic energy attributed to the momentum component normal to the surface [56]. There are several different types of sputtering. In case of the so-called *kinetic sputtering*, the transfer of the kinetic energy of the ion to the target surface leads to the ejection of particles. When an ion hits the target surface, a collision cascade is initialized, which transfers the energy not only onto the first layer but also to many atoms in the bulk [57]. For more highly charged ions also *potential sputtering* has to be taken into account, but only for non-conductive targets [41]. In this case, by removing electrons from an atom energy is stored. When interacting with the target surface the energy accumulated from higher ionization is released, resulting in a greater sputter yield than what is typically observed with purely kinetic mechanisms.

As a consequence, sputtering processes can lead to surface erosion and a change in surface composition. Due to the differing masses and surface binding energies of the atom species within a target, the energy transfer may vary even with the same incident ion beam. Therefore, certain atom species within the target are more readily sputtered than others, a phenomenon known as *preferential sputtering*. As one constituent erodes more rapidly, the less volatile species becomes enriched in the surface region, resulting in a change in surface composition depending on the applied fluence. This process continues until a steady state is reached, at which point sputtering proceeds according to the stoichiometry of the original bulk material [58, 59]. Due to its surface-changing properties, sputtering is often used for sample preparation. One application involves removing or modifying thin layers on substrates, while another utilizes it as a coating process in thin-film technology through magnetron sputtering [60, 61, 62]. During this thesis, sputtering was used to bring the samples to a state of equilibrium surface concentration to ensure well-defined and constant initial conditions before the electron irradiation experiments. Whether this is reached, can be checked by the Quartz Crystal Microbalance technnique.

2.2 Quartz Crystal Microbalance Technique

The Quartz Crystal Microbalance (QCM) technique is a well-established method for measurements of mass changes in real time and *in situ* using a quartz resonator. A particularly sensitive implementations has been employed at the Institute of Applied Physics (IAP) at TU Wien in the past years [29, 63].

The piezoelectric properties of quartz allow the accurate detection of mass changes during ion or electron bombardment. Two thin gold films on the resonator serve as electrodes, and an AC voltage is applied to induce a thickness-shear mode oscillation. Since there is a linear dependency between the mass of the resonator and its resonance frequency, this technique allows the determination of the sample mass change Δm by monitoring the change in the resonance frequency Δf over time. This relation is described by the Sauerbrey equation (2.1) when the initial frequency f_Q and the mass m_Q of the QCM are known [64].

$$\frac{\Delta m}{m_Q} = -\frac{\Delta f}{f_Q} \tag{2.1}$$

Furthermore, the mass change per unit area is defined using the density of the quartz ρ_Q, its thickness d_Q, and the area of the QCM A_Q:

$$\Delta m_a := \frac{\Delta m}{A_Q} = -\frac{\Delta f \cdot \rho_Q \cdot d_Q}{f_Q} \tag{2.2}$$

In addition, equation 2.1 is also valid if a thin layer of another material is applied on the quartz resonator, which has a thickness of around 300 µm.

Since the target is a component material and, in general, the absolute mass change per unit area is resolved, the contribution of the individual species in the target cannot be distinguished.

Another requirement necessary for the application of the Sauerbrey equation is that the incident beam current density, j, is constant over the sensitive quartz area. To ensure this, the incident beam is scanned and its current density is determined before and after irradiation. The number of incident charged particles on the QCM N_i in a time Δt is described with the help of:

$$N_i = \frac{j \cdot \Delta t \cdot A_Q}{q \cdot e_0} \tag{2.3}$$

Here, the charge state of the particle, q, and the elementary charge, e_0, are used. Therefore, the mass removal per incident particle, y, is defined by using the incident beam current density, j:

$$y := \frac{-\Delta m}{N_i} = \frac{\Delta f}{f_Q} \cdot m \cdot \frac{q \cdot e_0}{A_Q \cdot j \cdot \Delta t} \tag{2.4}$$

Using equation 2.2 one can express the mass m by the quartz density, thickness and area such that A_Q cancels:

$$y = \frac{\Delta f}{f_Q} \cdot \rho_Q \cdot d_Q \cdot \frac{q \cdot e_0}{j \cdot \Delta t} = \frac{\Delta f}{\Delta t} \cdot \frac{1}{j} \cdot \frac{\rho_Q \cdot d_Q \cdot q \cdot e_0}{f_Q} \tag{2.5}$$

The resulting formula can be divided into three components. The first, $\frac{\Delta f}{\Delta t}$, represents the gradient of the frequency-over-time curve. The corresponding values for this expression are obtained from the measurements. The second component is directly related to the incident beam current density, j. This part is also determined during the experiment using a Faraday Cup (FC). The final part is known as these are properties of the QCM.

Furthermore, the resonance frequency of the quartz crystal is very sensitive to temperature [65]. As a result, problems arise in distinguishing whether shifts in the resonance frequency result from changes in mass or changing temperature. When measurements are made under varying temperatures, variations due to temperature must be excluded. A common strategy to overcome this problem is to operate the quartz at an elevated temperature, where the resonance frequency reaches a minimum. At this point, fluctuations in temperature result in only minor alterations to the resonance frequency [29, 66]. The glowing filament of the electron flood gun constitutes a radiating heat source, which directed towards the QCM affects the resonance frequency of the quartz. With the established measurement procedure (see chapter 3), this issue was addressed and minimized.

2.3 ECR Ion Source "SOPHIE"

In the experimental setup, a 14.5 GHz Electron Cyclotron Resonance Ion Source (ECR Ion Source or ECRIS), known as *SOPHIE* (**SO**urce for **P**roduction of **H**ighly charged **I**ons using **E**CR), is used [67]. Via microwave radiation the plasma is ignited, heated and confined by an axial magnetic mirror field and a radial multipole field generated by a sextupole magnet. In the magnetic field, electrons perform cyclotron motion with a specific gyrofrequency and can absorb heating radiation resonantly in the range of their gyrofrequency. Further collisions between the electrons and the working gas lead to its ionization. An acceleration voltage of up to 10 kV can be applied to extract the generated ion beam. The previously extracted ion beam is further guided through an *accel-decel* system. This system contains three electrodes and is used to suppress electrons and further optimize the ion beam. The suppressor electrode is positioned between the extractor electrode, maintained at the ground potential, and the plasma electrode. A voltage of 2 kV can be applied between the extractor electrode and the suppressor electrode, while voltages up to 10 kV are possible between the extractor electrode and the plasma electrode. This is necessary to prevent electrons generated by the ionization of the residual gas or by collisions of the ion beam with the chamber wall metal from entering the plasma region.

2.4 Beam Line 3 (BL3)

Subsequently, the extracted ions are directed through *Beam Line 3 (BL3)*, where they undergo additional focusing before being guided into the experimental chamber. The initial phase involves the focusing of ions as they pass through two quadrupole magnets, each oriented at a 90° angle to the other. The generated magnetic field in this configuration exerts a Lorentz force on the ions, resulting in the focusing of ions along a particular direction in the plane perpendicular to the ion beam and defocusing along the other direction. Afterward, the ions are guided through a sector magnet that applies a constant vertical magnetic field. Within this magnetic field, the ions undergo circular motion along the vertical field lines. For a given magnetic field strength, the mass-over-charge ratio ($\frac{m}{q}$) of the particles determines the radius of the circular motion. It is important to note that the mass-over-charge ratio is directly proportional to the square of the magnetic field strength (B^2). This property enables the selective deflection of ions with specific m/q ratios into the desired beam path, while simultaneously diverting unwanted charge states or ion species. Following the sector magnet, a removable Faraday cup is installed, which facilitates the pre-adjustment of the ion beam and further gives the possibility to take mass over charge spectra by ramping up the sector B field as a means of analyzing the ion species present in the plasma. Subsequently, the ion beam is steered through a pair of deflection plates, allowing it to be dumped into one of the plates and thereby electronically starting and switching off phases of irradiation. Afterwards, the beam proceeds through two sets of beam optics, each consisting of an aperture, two pairs of deflection plates, and an einzel lens. One of the apertures in this configuration, called L1, is connected to a picoammeter that is used to measure the incident ion beam current and consequently helps to direct the ion beam. In the initial stage of guiding the ion beam into the experimental chamber, an operating point for the quadrupole magnet and sector magnets are determined by maximizing the current recorded at L1. Subsequently, the ion beam is focused and directed through L1 using the first set of deflection plates and the first lens. In the subsequent step, the second set of beam optics is employed to maximize the beam current within the Faraday cup in the target chamber. Furthermore, the focused ion beam can be scanned over the target area by employing a pair of scanning plates positioned in front of the chamber entrance. The purpose of scanning the ion beam is to maintain a constant current density across the entire sensitive quartz surface. On the one hand this ensures that the Sauerbrey formula 2.1 can be applied for ion sputtering studies and it ascertains that the whole sample area is cleaned when using ions for sample preparation on the other hand.

2.5 Experimentation Chamber

In the experimental chamber, the sample holder, as illustrated in Figure 2.1, serves as the central part, and its main components are distributed within three compartments, which are explained below. As previously mentioned, the ion and electron beam current is monitored using a Faraday cup. Positioned on the manipulator, the Faraday cup is capable of movement in the experimentation chamber and rotatable, enabling detailed examination of the geometry of the incoming electron or ion beam. Additionally, a suppressor is placed in front of the Faraday cup to mitigate the distortion of current measurements caused by secondary electrons released from the inner wall of the Faraday cup due to ion impact. Concerning an incoming electron beam, the suppressor's negative potential of -3 V hinders electrons with energy below the specified potential from entering the Faraday cup.

Located in the second compartment on the sample holder is a quartz resonator acting as a QCM. On the QCM a thin layer of the sample material is deposited. By bombarding these amorphous thin films with particles such as ions or electrons, the material's response to the charged particle irradiation in the form of mass change is studied. Furthermore, by rotating the sample holder around its central axis, the dependence of, e.g., the sputtering yield on the incidence angle can be further examined.

The last compartment hosts space for samples from bulk materials. Interesting sample properties are often not transferable to a thin film on a quartz resonator. Such characteristics include crystallinity, roughness or special nanostructures, among others, and their inclusion often represents a step further towards samples more representative for their desired application. In the recent past, these kind of bulk specimens have been investigated at the IAP by collecting their sputtered ejecta by means of a second dedicated QCM. From these experiments, it was possible to deduce the sputtered ejecta angular distribution of fuzzy W samples relevant for nuclear fusion reactors [68] and the sputtering yields of rough mineral pellets more analogous to the hermean and lunar surfaces [31].

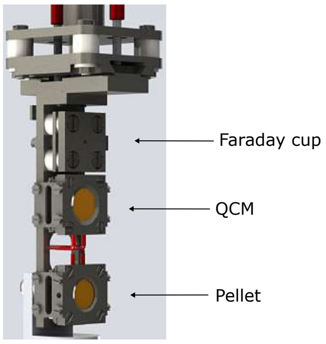

Figure 2.1: 3D Visualisation of the target holder as main component in the experimental chamber. Underneath the Faraday cup, the quartz sample is mounted to analyze the amorphous thin films. To further investigate the sputter yield of polycrystalline samples, a pellet can be mounted in the third compartment.

Additional stepper motors allow the movement of the target holder along three axes (x, y, z) and rotation (α) around its center axis in the experimental chamber. In Figure 2.2 the position of the target holder, represented by the QCM in the second compartment, is illustrated. In addition to the ion beam, whose extraction from the ion source has been previously elucidated in greater detail and primarily serves the purpose of cleaning the QCM before actual measurements, an electron beam is required for the observation of ESD. This electron beam is generated using a Flood gun *FS40A1* manufactured by the *PREVAC* company, positioned at an angle α of 45° with respect to the incoming ion beam, and located at a distance d of approximately 7 cm.

In addition, several cables connect form the sample holder to the outside of the chamber. Starting with the cables for the QCM electronics, suppressor and for the current measurements in the FC also a K type thermocouple and heating wires are employed to heat both the QCM and the pellet.

Moreover, for the experiments conducted in the chamber, an ultrahigh vacuum (UHV) pressure range is required. To achieve this, two ion getter pumps and a turbomolecular pump are utilized. Combined with two scroll pumps as backing pumps alongside a titanium sublimation pump, a typical pressure in the range of 10^{-10} mbar can be achieved.

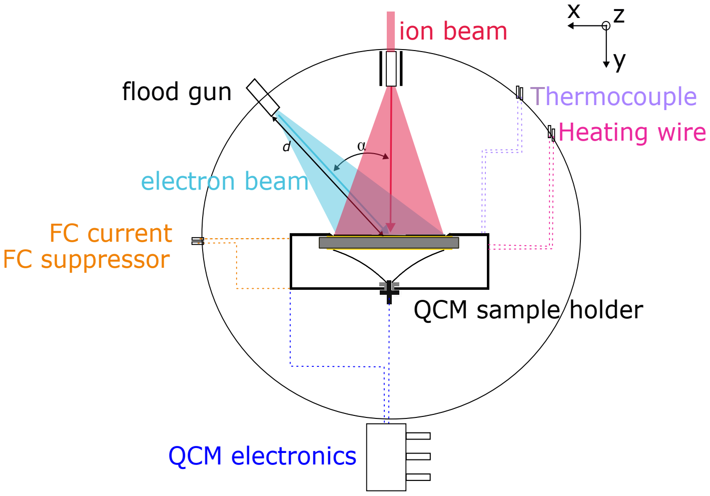

Figure 2.2: Arrangement of the target holder represented by the QCM in the experimental chamber and the incoming electron and ion beam. The angle α between the electron beam and the ion beam is set to 45 degrees. The target holder can be moved along three centre axis and can also be rotated around its axis. Several cables for the QCM electronics, the FC current, the FC suppressor, Heating wires and thermocouple connect to outside of the experimental chamber.

2.6 Flood gun FS40A1

In the experiments conducted, the *PREVAC Flood Source FS40A1* serves as the electron source. In this source, a heated tungsten cathode is employed to supply electrons via thermionic emission. The electron emission current is adjustable within a range spanning from 0.1 to 1000 µA and is regulated by manipulating the heating current. Furthermore, the energy of the emitted electrons can be varied within a range of 0 to 1000 eV. As shown in Figure 2.3, the released electrons are extracted in one direction by an extractor voltage up to +150 V. Subsequently, the generated electron beam is focused using a voltage within the range of +300 to +1000 V.
Additionally, the flood source has a pre-set stand-by mode, in which no voltage and no emission current are applied. Due to these parameter settings, no electrons are extracted. Also, by reducing the emission current to 0 μA (while keeping extractor, focus and energy voltages active), the emission of electrons can be minimized. A third option to diminish the electron current from the flood gun is by setting the extractor voltage to 0 V, in this case electrons are emitted from the cathode but remain unaccelerated. The influences on the quartz resonance frequency of these possibilities to switch the electron current off and their implications for measurements shall be explored in the following section.
Furthermore, the values for the focus and extractor voltage during the later performed measurements are also shown in Figure 2.3 .

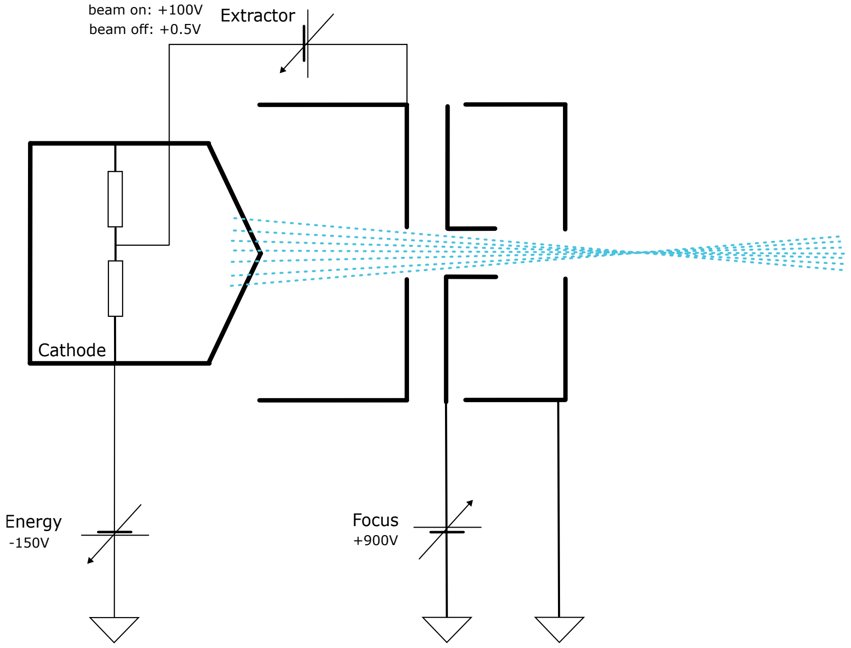

Figure 2.3: Diagram of the utilized Flood source *FS40A1*. In this instance, electrons are emitted through thermionic emission and subsequently accelerated and focused by applying different voltages, which can be regulated while operating the flood source. Typical values for the extractor and focus voltage at an electron energy of 150 eV are shown.

2.7 QCM Electronics and Controlling

Via tracking of the resonance frequency of the quartz, information about mass change rates is gained. For this purpose, specialized electronics were utilized. A voltage controlled oscillator and a fast circuit are connected via a signal, power and feedback line. The fast circuit is further directly attached to the vacuum chamber and is the connection between the quartz and the oscillator. Since a feedback voltage depending on the phase shift of the current through the quartz is generated, it is also called phasebox. The output signal of the phasebox now depends on the actual resonance frequency of the quartz and the input frequency of the oscillator. A low noise oscillator with a tunable frequency between 59 and 96 MHz is used. This oscillator output is directed to both a frequency counter used to log the frequency and a Johnson counter to divide it by a factor of 10 [69]. Afterwards the sinusoidally shaped output of the oscillator is directed to the phasebox. The circuit of the phasebox is shown in Figure 2.4.

Generally, the circuit is composed of two branches, in which the quartz is connected to Pin 12 of IC2, facilitating differentiation between the two branches. The RF current passes a 47 pF capacitor resulting in a phase difference between the two branches when the quartz is resonant. If the quartz is in resonance the phase shift is 90 degrees and this leads to a zero voltage output. Alternatively, if there is a non-zero DC voltage, controllers will synchronize with the output's zero crossing.

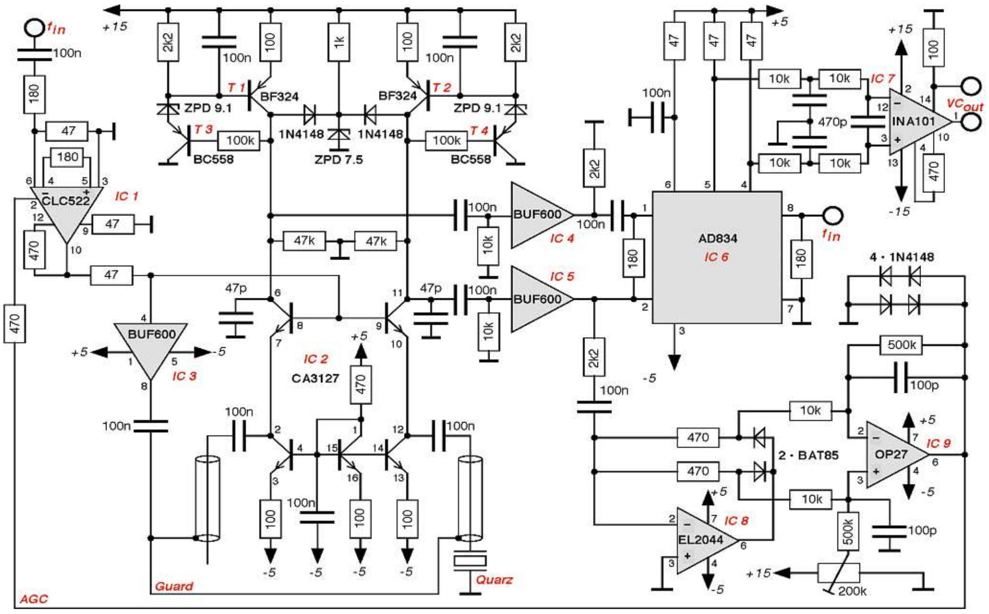

Figure 2.4: Circuit of the phasebox

Over the years, various components from the original circuit diagram have been substituted. An overview of the repair work is given in [70].

3 Standardized Measurement Procedure

In the subsequent chapter, the process behind the establishment of the measurement procedure used in the experiments discussed in the following is explained. The aim was to reliably switch the electron beam on and off with as little perturbation to the QCM resonance frequency stability as possible.

3.1 Controlled activating and deactivating of the flood gun

According to the manual of the flood gun a period of around 4500 s is required until a stable electron beam is generated once the device is activated. This activation also influences the QCM resonance frequency. Therefore, the primary focus was to develop a method for precisely activating and deactivating the electron beam in order to have knowledge about the total electron irradiation time (and thereby also the applied electron dose) without disrupting the QCM resonance. The electron current should immediately drop to zero when the flood gun is switched off and reach its stable equilibrium value when switched on without delay or any further waiting time. Various parameters, such as the pre-programmed stand-by mode, the emission current, and the extractor voltage, can be used to minimize the electron flow of the *FS40A1* flood gun.

Each possible method for activating and deactivating the electron beam was tested using the same parameters to ensure comparable results. In the search for a measurement procedure, the flood source is operated with an extractor voltage of +60 V, a focus voltage of +1000 V, an emission current of 300 µA and electrons with an energy of 20 eV are extracted.

After a warm-up phase of 5000 s, the flood gun is switched off for increasing periods of time, varying a single parameter at a time. After this period, the manipulated parameter is reset to the initial values and the flood gun is operated with the normal settings for 10000 s before the next period is examined. This procedure is carried out for intervals of 60, 30, 20 and 10 minutes. During the measurement procedure, the quartz resonance frequency, the current of the incoming electron beam in the Faraday cup and actual values of the flood gun parameters are recorded.

3.1.1 Stand-by Mode

The standby mode originally intended for this purpose was selected as the first option for activating and deactivating the electron beam. In this pre-programmed mode, the emission current, the electron energy, the focus voltage and the extractor voltage are set to zero. The actually measured values reported by the flood source controller are 0.2 V for the electron energy, 0.4 V for the focus voltage and +2.7 V for the extractor voltage; For simplicity zero values will be used in the following. With these settings, no electrons are emitted, and therefore no electron beam is formed. Since the focus voltage is reduced to 0 V in the stand-by mode, this is used as a proxy to indicate whether the stand-by mode is active or not. The focus voltage, the measured electron current in the FC and the change in the resonance frequency and their change over time are plotted in Figure 3.1. During the normal operation time (focus voltage is set to +1000 V) the frequency steadily decreases, as shown in Figure 3.1a. As soon as the stand-by mode is activated the trend in the recorded frequency changes and it starts to rise. The electron current in the Faraday cup constantly increases, up to -400 nA, when the flood gun is running, see Figure 3.1b. Once the flood gun is switched to stand-by, the current instantly drops to about -25 nA. When comparing the electron beam current and the focus voltage (Figure 3.1c), it is observed that the electron current does not react instantly when the flood source is switched on. Depending on how long the flood gun has been in stand-by mode, it can take up to 5000 s to start rising again. Only for the shortest switched off duration of 10 min the electron current instantly returns to its previous values.

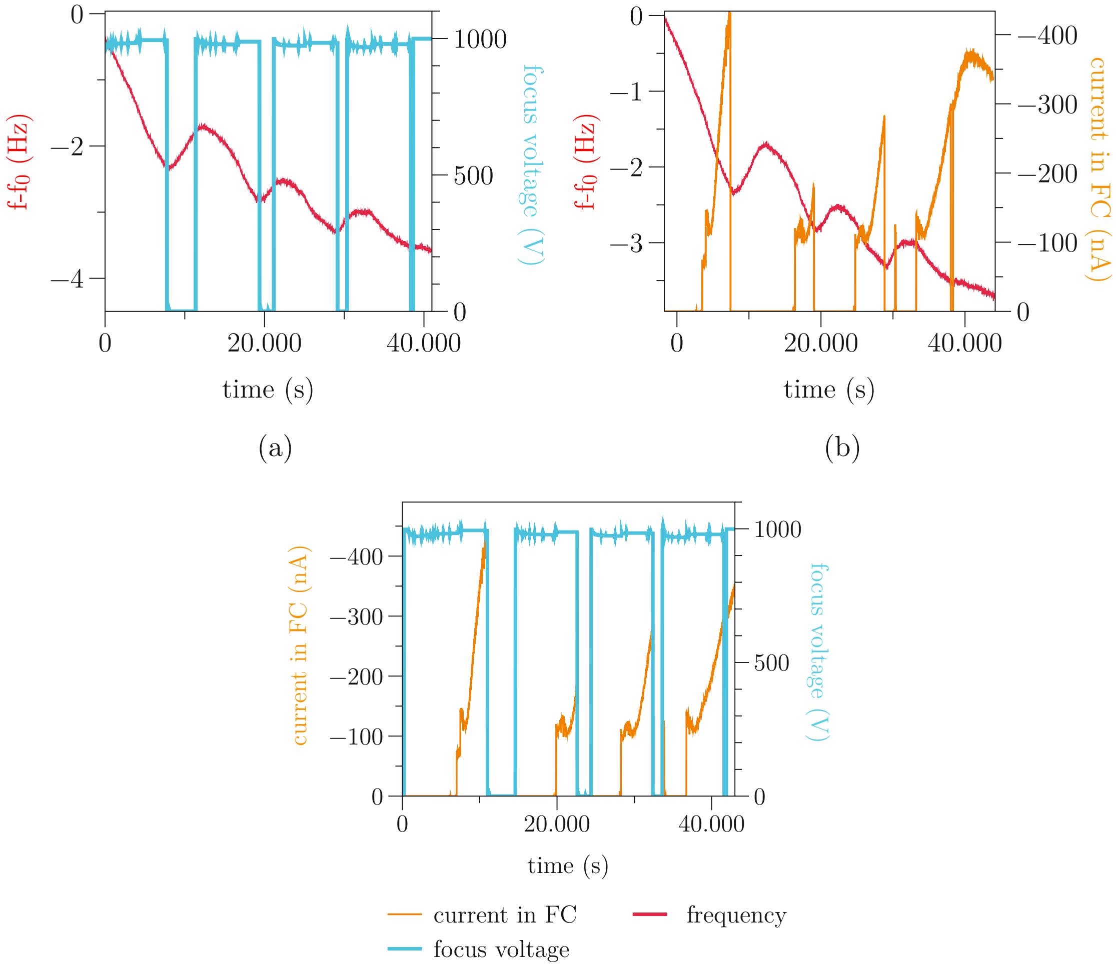

(a)

(b)

(c)

Figure 3.1: Recorded quartz resonance frequency (a) and electron current (b) measured in the Faraday cup, while the flood gun *FS40A1* was switched between operation and stand-by mode for different time intervals (c). The focus voltage is shown, which is equivalent to whether the flood gun is in stand-by mode (focus voltage is set to 0 V) or is being operated normally (focus voltage is +1000 V). It can be seen that the quartz resonance frequency is constantly decreasing except for the time period when the flood gun is in stand-by mode. Furthermore, the electron current increases over time when the flood gun is used, but needs about 5000 s each time the stand-by mode is deactivated until an electron current is detected.

The observed decrease in the resonance frequency of the QCM while the flood gun was in the stand-by mode is consistent with the behavior typically associated with temperature changes [65]. Based on previous experiments [22], it was noted that as the quartz temperature rose, there was a corresponding decrease in the quartz resonance frequency, in agreement with both the qualitative trends and quantitative measurements observed in this experiment.

The extended duration required for both the measured electron current and resonance frequency of the quartz to stabilize after the switch to stand-by mode would further affect the measurements as an additional background signal and adds significant uncertainty to the applied electron dose. With these background signals the mass changes caused by electron irradiation could not be reasonably resolved. Therefore, the standy-by mode is not suitable for switching the electron beam on and off and the manipulation of other parameters is tested in the following.

3.1.2 Emission Current

It is also possible to reduce the electron current to around -20 nA by changing the emission current from 300 µA to 0 µA. This possibility along with its implications on both QCM resonance frequency and extracted electron current was tested using the same method as in section 3.1. During the procedure, the resonance frequency of the quartz decreases steadily while the emission current was set to 300 µA. As soon as the emission current was reduced to zero, the frequency instantaneously changed this trend and started to increase. This behavior was observed for each reduction in the emission current. Restoring the emission current to 300 µA did not immediately alter the resonance frequency trend, see Figure 3.2a. Only after a few hundred seconds a noticeable change became apparent. Alterations in the emission current were observed within the experimental chamber as well. As the emission current was reduced to zero, a corresponding decrease in the light within the flood gun aperture was observed. The change in the resonance frequency of the quartz and the visible effect in the experimental chamber can be both attributed to the thermal input of the glowing filament within the flood source.

Looking more closely at the electron current measured simultaneously with the Faraday cup as illustrated in Figures 3.2b and 3.2c, it was found that the electron current required 3500 s to start rising again after switching off. Furthermore, it rose continuously up to values of -500 nA and only decreased to -20 nA again because of the shutdown process. During the last shutdown of 10 min, no prolonged drop in the electron current values was recorded. The values before and after switching were also comparable. However, a subsequent reduction in electron current was observed while the flood gun was continuously operating at 300 µA.

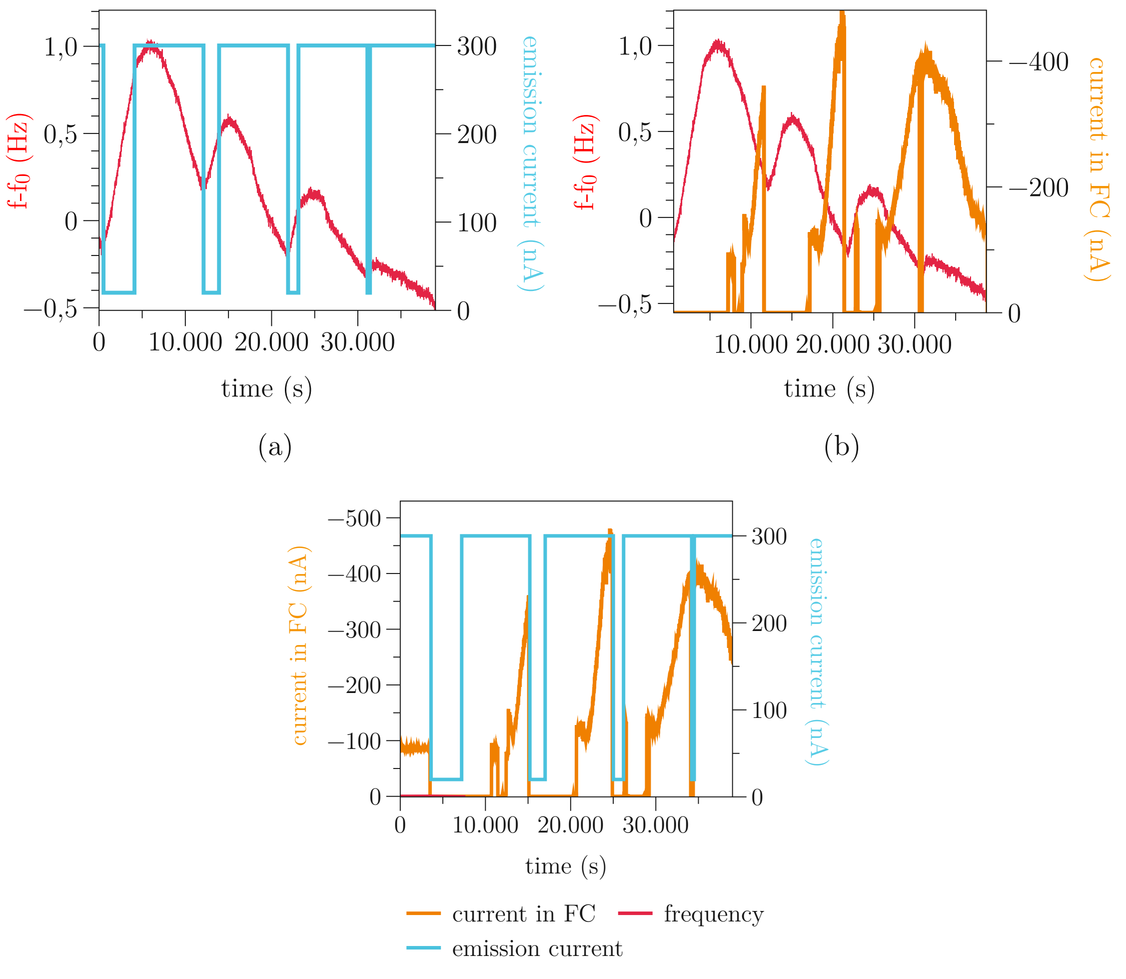

(a)

(b)

(c)

Figure 3.2: Recorded quartz resonance frequency (a) and electron current (b) in the Faraday cup while the emission current is switched from 300 µA to 0.1 µA for different duration. The recorded resonance frequency decreases steadily while the flood gun is normally operating. As soon as the emission current is set to 0 µA this trend changes. Also, the recorded electron current in the Faraday cup drops to -20 nA when the emission current is reduced (c). After the emission current is set back to 300 µA about 3500 s are necessary for the current in the Faraday cup to rise again.

3.1.3 Extractor Voltage

In the following stages, the extractor voltage is lowered from +60 V to +0.5 V to minimize the electron current. It should be highlighted that the extractor voltage was intentionally not reduced to the lowest feasible value accepted by the flood source controller of +0.1 V, as the emission current of 300 μA can no longer be achieved and this results in the flood gun being switched off.

Examining the quartz resonance frequency over time revealed a consistent decline in the initial 25000 s, even during the period when the extractor voltage was minimized for 60 min, as illustrated in Figure 3.3a and 3.3b . During subsequent time intervals with reduced extractor voltage of 30 and 20 minutes, respectively, a rise in the quartz resonance frequency was observed. However, it is important to note that the detected increase was only 0.04 Hz and 0.02 Hz over the respective time periods. The obtained values can further be converted into gradients of 1.3 mHz/min and 1 mHz/min which corresponds to typical values for drifts in the QCM resonance frequency [29]. At 25000 s the resonance frequency started to rise even in the time when the flood gun was operating normally.

Furthermore, the electron current in the Faraday cup was monitored, revealing a stable and constant flow of -80 nA during the regular flood gun operation. By lowering the extractor voltage, the electron current within the Faraday cup was reduced to -25 nA, see Figure 3.3c. When the extractor voltage was increased to +60 V, an instantaneous effect on the measured electron current was evident. The observed electron current remained comparable to values recorded before the switch. It should be mentioned that by reducing the extractor voltage the electron current is minimized but the electron energy remains at the selected energy.

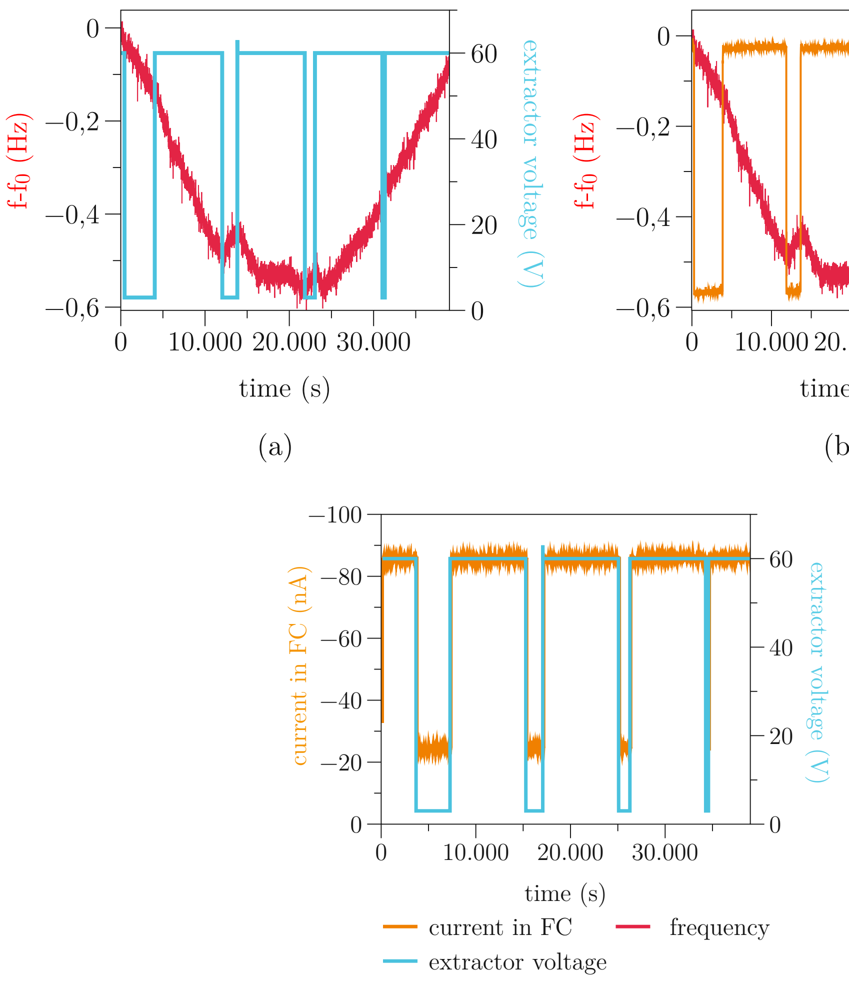

(a)

(b)

(c)

Figure 3.3: Recorded quartz resonance frequency (a) and electron current (b) while switching the extractor voltage between 0.5 V and 60 V. By manipulating the extractor voltage, no significant change in the trend of the recorded resonance frequency was detected. It is notable that the electron current changes exactly at the time when the extractor voltage is varied (c). Reducing the extractor voltage results in a decrease in the electron current to approximately -25 nA.

In summary, an instantaneous response in the measured electron current was detected to the change of the extractor voltage. Furthermore, the temporal behavior of the electron current in the two settings (on and off) was constant over time. Combined with the fact that the QCM resonance frequency is influenced such that changes in mass can still be determined with the usual precision, this method seems very promising.

3.2 Established Measurement Method

In the previous subchapters, various parameters were examined to identify a possible mechanism to switch the *FS40A1* flood gun on and off. The goal was to find a mechanism that has minimal or no impact on the quartz resonance frequency and exhibits immediate responsiveness upon activation and deactivation. The extractor voltage exhibits minimal interference with the recorded quartz resonance frequency, and the electron current promptly responds to any changes in the operational state of the flood source. Furthermore, elevating the extraction voltage to +100 V resulted in an increased electron current compared to the -80 nA measured during the flood gun operation time in subchapter 3.1.3. By adjusting the extractor voltage to +0.5 V to turn off the electron beam, a 60-minute window is created during which the flood gun can be switched off without impacting the frequency or altering the electron current when it is turned back on. During this time the ion beam can be examined and subsequently used to clean the quartz before the electron irradiation.

It is additionally mentioned here that an effort was made to raise the extractor voltage to its maximum value of +150 V. However, these attempts led to the issues that in certain instances, the emission current could not be attained, and concurrently, the cathode underwent persistent strain such that repair work was necessary twice.

In the next phase, a standardized measurement procedure is developed. To ensure the stability of the QCM resonance frequency and prevent any influences from the activation of the flood gun, a duration of 5000 s is waited after the electron source is switched on for the first time and before the actual measurement is carried out. During this time, the quartz resonance frequency and the electron current in the Faraday cup are already recorded. Subsequently, the target holder, as shown in Figure 2.1, can be adjusted along the z-axis, with its position and elevation is defined by the plane formed by the electron and ion beam. In the next step, the target holder is moved to the FC position and the electron current is measure for 500 s while the flood gun is normally operating while the extractor voltage is set to 100 V. Next the electron beam is turned off by setting the extractor voltage to +0.5 V and any residual electron current in the Faraday cup is documented. To ensure that the surface of the quartz is free from contaminants, the target holder is rotated by 45° into a 2 keV Ar^+ beam and cleaned for 1000 s. In this duration, a stable sputter yield is ensured by tracking the QCM frequency. With this, optimal conditions are maintained concerning the surface characteristics of the sample.

After the cleaning procedure, the extractor voltage is set to +100 V, and the target holder is rotated back into the electron beam. Before proceeding, the electron current is measured at the Faraday cup position to ensure it has not changed during the cleaning process. Finally, the target holder is maneuvered to the QCM position, and the actual measurement is executed.

Additionally, a *background* measurement was performed to observe the behavior of the quartz frequency without the operation of the flood gun. In this measurement, the extractor voltage of the flood gun is switched off by means of the extractor voltage, while the rest of the process remains unaltered. The aim was to verify that this newly established experimental procedure in its entirety does not perturb the QCM resonance frequency beyond the usually observed frequency drifts.

4 Results and Discussion

In this chapter the measured data is presented and further analyzed. In the beginning the electron beam is characterized followed by the determination of the energy threshold and the mass erosion per incident electron for the $MgSiO_3$ sample. For a better comparison, the energy threshold and the mass ejection were also determined for an Au and a LiF sample.

4.1 Electron Beam Stability

Before proceeding with the irradiation of the quartz, the generated electron beam was examined to ensure its stability during operation and to verify that the sensitive area, which has an effective radius of approximately 2-3 mm around the center of the quartz, is evenly irradiated with a constant electron current. In this context, two beam profiles were taken with a time difference of three hours, roughly equal to the duration of one ESD measurement. The beam profiles recorded in this context are shown in Figure 4.1.

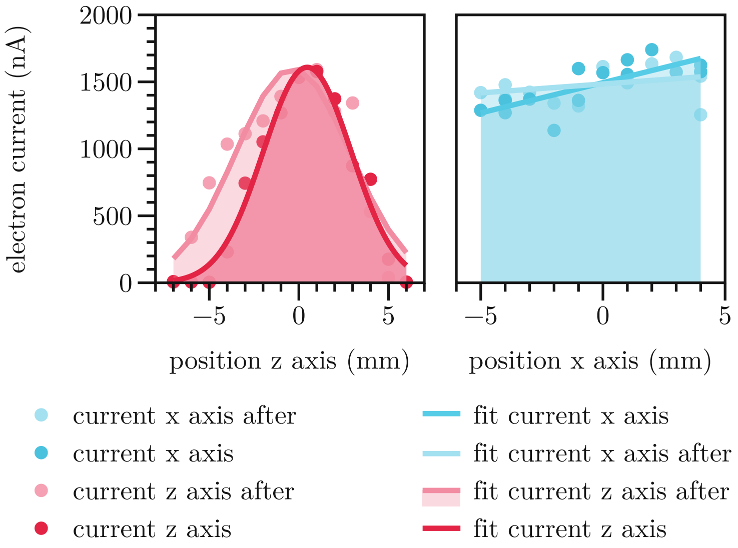

Figure 4.1: Recorded profiles of the electron beam with a time difference of three hours in between. Slight differences in the detected beam profiles were observed. Furthermore, a nearly constant electron current in the x-y plane and a decrease in the electron current around the center of the QCM in z-axis were visible.

In general, only a relatively small shift in the recorded beam profile was detected in both the z- and x-axis. For a better comparison the electron current in the coordinate system relative to the incident ion beam can be seen in Figure 2.2. On closer examination of the beam profile of the z-axis, a decrease in the measured electron current was observed at a distance of 2 mm around the sensitive centre of the quartz. Furthermore, the electron current drops nearly to zero at ± 5 mm offset of the center. Since the distance along the z-axis between the FC and the QCM centers is 21 mm, it is ensured that only a negligibly small amount of electron current, if any, is applied to the QCM while measuring the current with the FC.

Along the x-axis a nearly constant electron current was detected on the examined area. Furthermore, the maximum of the measured current on the z-axis is comparable to the values measured in the x-y plane. Since the radial sensitivity of a QCM corresponds to a Gaussian distribution around the sensitive center, the electron current applied further than 2 mm from the center will have little effect on the measured change in resonance frequency. Therefore, the decrease in the z-axis at 5 mm offset is not of interest and the average electron current and the standard deviation applied onto the sensitive area of the quartz can be calculated.

For the z-axis this results in an average electron current of 1360 nA and a relative error of 6.9%, respectively for the x-axis in an average electron current of 1517 nA and a relative error of 4%. This relative error of the electron beam current is later used in the calculation of the mass removal. With this stable and constant electron current in the sensitive quartz area, the flood source *FS40A1* provides a useful electron source for the following measurements. Next, the impact of electron irradiation on the lunar analog material enstatite will be examined.

4.2 Enstatite ($MgSiO_3$) Sample

Enstatite serves as an analog material for both Moon and Mercury, however little data regarding the behavior of $MgSiO_3$ under electron irradiation is available. Information from other materials indicates the existence of an energy threshold for ESD processes. In the first step, information concerning the energy threshold is presented before the detected mass removal as a result of electron irradiation is shown.

4.2.1 Energy Threshold

From an initial electron energy of 10 eV, subsequent measurements and background measurement were performed in the energy range up to 50 eV. Since no significant difference in the frequency of the background measurements and the performed sweeps for electron energies lower than 50 eV was observed, the values are not shown for simplification. During the experiments with an electron energy of 50 eV a first difference between the background measurement and the performed irradiation was observed, as shown in Figure 4.2.

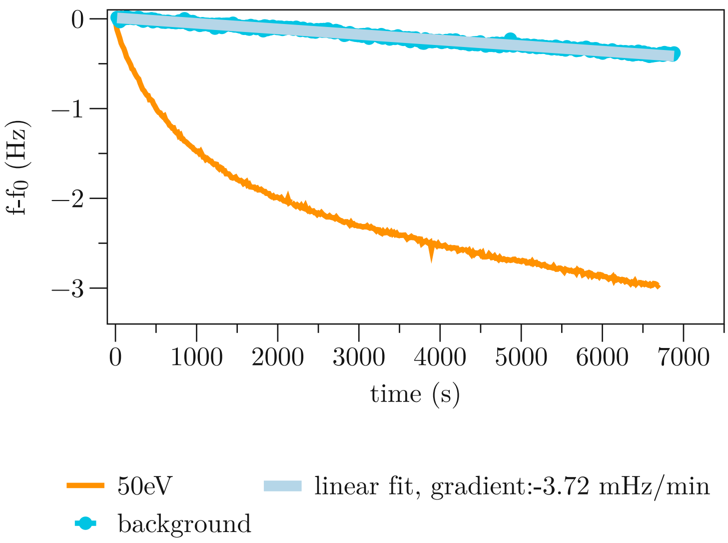

Figure 4.2: Recorded resonance frequency during electron irradiation with an energy of 50 eV. Additionally, the results for the background measurement are presented. The resonance frequency at 50 eV decreases steadily, which could not yet be recorded at lower energies. For these lower energy cases, no significant difference in the resonance frequency of the background measurements and the actual irradiation is detected.

During the irradiation time of 7000 s a total frequency change of -3 Hz is observed. The background measurement also shows a steady decrease in frequency. Fitting a linear model to the background measurement data, a gradient of −3.72 mHz/min was calculated, which corresponds to a typical quartz frequency drift when the QCM is not manipulated [29]. Since up until this energy, no frequency increase and therefore no mass reduction is detected, the energy of the electron beam was further increased up to 300 eV, see Figure 4.3. Also for the higher electron energies up to 300 eV addition background measurements were performed. Since no significant change compared to the background measurement at 50 eV was observed, these curves are not shown.

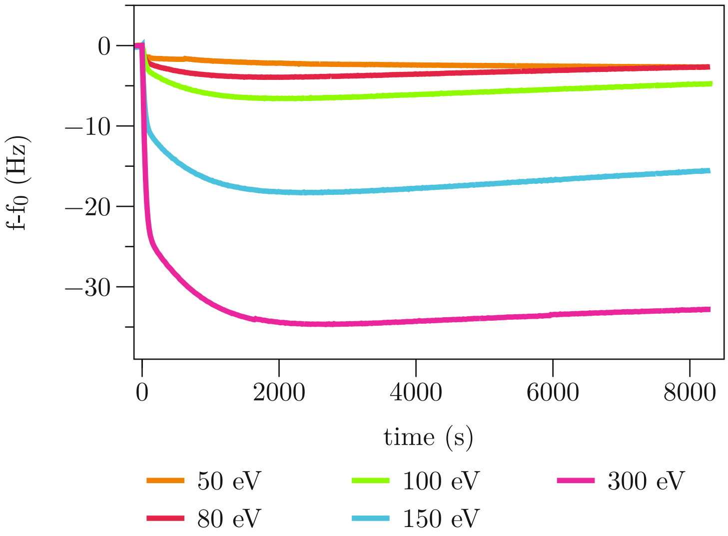

Figure 4.3: Recorded resonance frequency during ESD measurements with electron energies up to 300 eV. For the energies greater than 50 eV, an initial drop in the resonance frequency was recorded. For higher electron energies after reaching a minimum also an increase in frequency was recorded, which corresponds to a detected mass erosion of the quartz.

At an electron energy of 80 eV, a more substantial drop in the resonance frequency compared to the 50 eV curve is observed. However, after reaching a minimum, an increase is observed for the first time, which according to equation 2.1 corresponds to a mass erosion. A similar trend is recorded for electron energies of 100 eV, 150 eV and 300 eV. Furthermore, an additional measurement was performed with an electron energy of 500 eV. In the course of this experiment a qualitatively similar trend compared to the 100 eV, 150 eV or 300 eV measurements was observed. Since the minimum at the beginning was observed at around -100 Hz compared to the initial resonance frequency of the quartz, the detected rise of a few Hz during the irradiation time is relatively small. To give a better insight of the resonance frequency trend the recorded curve at 500 eV is not shown in Figure 4.3. In the following a corresponding mass removal for each performed measurement is calculated.

4.2.2 Mass Removal

As already shown in Figure 4.3, differences in the gradient of the resonance frequency curves for the enstatite sample are visible. In general, the observed gradient varied for each electron energy and also for each measurement. Since this variation might be due to the different electron current for each measurement, the gradients were normalized to the number of electrons and the mass removal per 1000 incident electrons was calculated in order to eliminate the influence of the electron current.

The resulting values are illustrated in Figure 4.4.

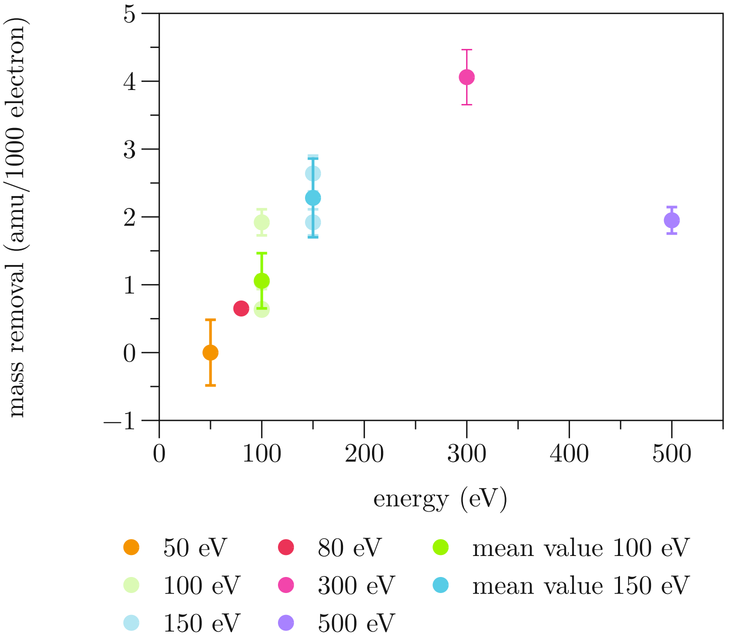

Figure 4.4: Calculated mass ejection per 1000 incident electrons for each measurement with used electron energies up to 500 eV. Starting at an energy level of 80 eV, a net mass removal was detected. Subsequently, the average value for the mass removal increases up to an electron energy of 300 eV.

As indicated in Figure 4.2, no mass erosion was recorded at an electron energy of 50 eV. However, with an increase to 80 eV a mass ejection of roughly 0.65 amu/1000 electrons was detected and increased up to a mean value of 4.06 amu/1000 electrons at 300 eV. Furthermore, a decrease to 1.95 amu/1000 electron was observed at 500 eV energy of the incident electrons.

Despite fluctuations in the individual measurements, the calculated mass removal per 1000 incident electrons seems to increase with higher electron energies up to an electron energy of 300 eV.

4.3 Gold Sample

Since there are limited data available to compare the determined mass removal for the enstatite sample with literature values, it is not possible to verify the functionality of the established measurement procedure presented in 3.2. For further comparison, measurements using a gold sample were performed. Gold is an effective conductor where disturbances and excitations are rapidly dissipated within the electronic system. Furthermore, Aumayr and Winter associated the mechanism of potential sputtering with the mechanism discussed for ESD, neither of which occurs in gold [41]. Consequently, a gold sample is utilized as a reference to demonstrate what the quartz signal should look like if no ESD takes place. The resulting curves for an electron energy of 80 and 300 eV are shown in Figure 4.5.

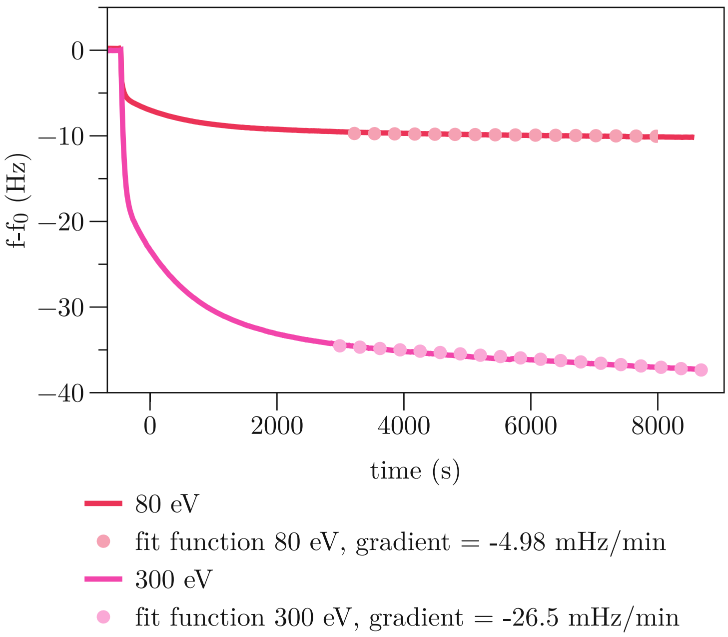

Figure 4.5: Observed resonance frequency change under electron bombardment of a gold sample with 80 eV and 300 eV. In the beginning a steep drop in the recorded frequency trends is visible followed by a steady decrease of about 4.98 mHz/min respectively 26.5 mHz/min.

For both measured curves a steep drop at the begin of the electron irradiation is visible, comparable to the one observed in Figure 4.3. At the higher energy of 300 eV, a more substantial decrease of around 35 Hz was observed compared to the 8 Hz drop for the 80 eV measurement. Following that drop, a steady decrease in the recorded resonance frequency for both electron energies is observed. The absolute value of the gradient of the QCM resonance frequency as a function of time is observed to change and decreases. After roughly 3000 s for attenuation, a linear fit was performed. The resulting slopes from the fitted functions for each irradiation vary from -4.98 mHz/min for an electron energy of 80 eV to -26.5 mHz/min for 300 eV. The observed drift in resonance frequency for the 80 eV measurement corresponds to typical values reported by Hayderer *et al.* in [29] when the QCM is in idle. For the 300 eV experiment, the reported slope is still not in this regime. However, the gradient is not yet stable over the fitted time interval, resulting in a fit worse than in the 80 eV case. If shorter and later time intervals are considered, the steepness decreases further. After the more pronounced drop, a longer attenuation time is therefore necessary to recover a stable quartz signal. Nonetheless, since no increase in the resonance frequency was detected during the irradiation time, also no mass desorption was observed in both cases. This conduct aligns with the initial assumption that no electron-stimulated desorption should be detected.

4.4 LiF Sample

While no electron-stimulated desorption is observed with gold as expected, LiF should serve as a contrasting example. As an alkali halide, LiF is known for showing both potential sputtering and ESD processes [41, 39, 40, 47]. Additionally, it can be deposited as a thin film on QCM's and is therefore also very suitable for testing the feasibility of the methodology.

4.4.1 Energy Threshold

After comparison with existing literature data, initial values of 20 eV, 50 eV and 80 eV were selected as electron energy and the experiments were performed at room temperature at around 22° [48]. The resulting resonance frequency changes during the measurement procedure are visible in Figure 4.6.

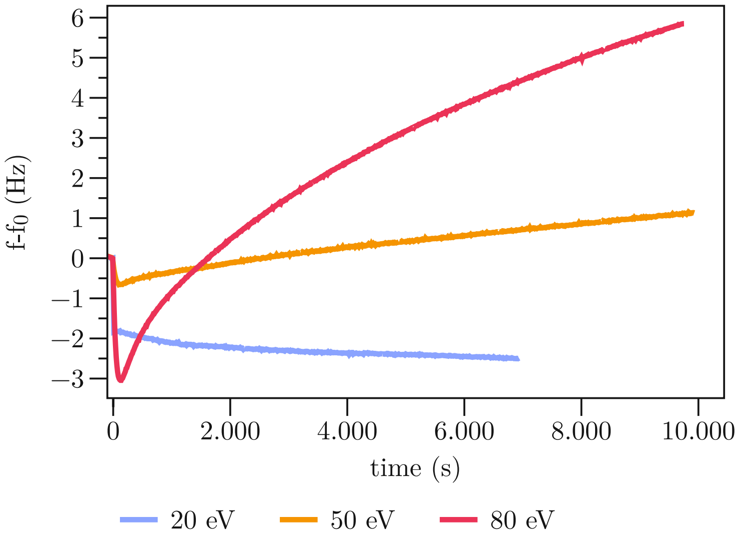

Figure 4.6: Resulting resonance frequency changes during the performed electron irradiations using LiF as a target. After comparison with existing literature data energy for the electrons 20 eV, 50 eV and 80 eV were chosen [48].

In the beginning the effects of electron irradiation with an electron energy of 20 eV were observed. In this case a steep decrease of around 2 Hz in the resonance frequency of the quartz is observed in the first 60 s. Afterwards, a steady decrease in the resonance frequency is detected. For the 50 eV curve, a drop in the frequency curve was detected at the beginning of the measurement procedure, leading to a minimum in the recorded resonance frequency after around 300 s. In the following irradiation time of 10000 s, a 1 Hz increase in the frequency was detected. A similar tendency was visible for the 80 eV curve. However, the minimum at the beginning of the measurement is with 3 Hz also lower and the followed increase in the resonance frequency is comparatively steep, especially right after the minimum. This measured increase at 50 eV is corresponds to a mass depletion. With this measurement, an energy threshold for desorption of LiF can be deduced to lie between 20 eV and 50 eV. It should be mentioned that also in the case of LiF background measurements were performed, since no significant changes in the resonance frequency compare to 4.2 was observed, these curves are not shown.

4.4.2 Mass Removal

Since a mass ejection was detected for electron energies greater than 50 eV, the gradients of the individual curves will be examined more closely and the mass removal per 1000 incident electrons is evaluated. For the 80 eV measurement, illustrated in Figure 4.6, also a time resolved mass removal per 1000 incident electrons was calculated, which is shown in Figure 4.7.

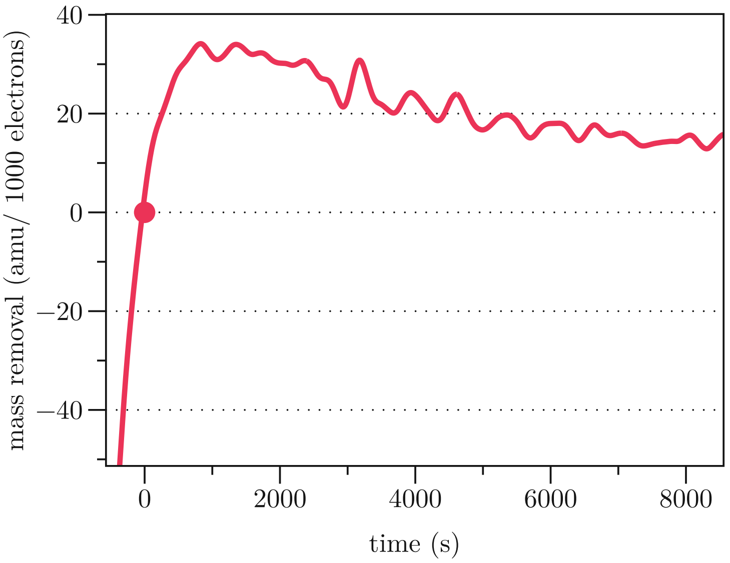

Figure 4.7: Time resolved mass removal per 1000 incident electrons for an electron energy of 80 eV on LiF. The highest values are detected within the first 2000 s after the minimum in the resonance frequency (red dot), before the mass ejection gradually stabilizes to a constant level.

After the recorded minimum in the resonance frequency of the 80 eV curve, indicated by the red dot, a net mas removal was first recorded. At the highest rate, a mass removal of about 35 amu per 1000 incident electrons was detected. As the irradiation progressed, the rate of mass ejection stabilized, reaching a consistent level of around 15 amu per 1000 incident electrons.
Due to the flatter gradient in the 50 eV experiment already illustrated in Figure 4.6, a mean mass removal over the irradiation time was calculated. This resulted in an average mass reduction of 2.74 amu/1000 electrons.

To further evaluate the mass ejection of the LiF sample, additional measurements with an electron energy of 80 eV were performed to obtain better statistics. In course of these following experiments a steady decrease of the detected mass removal was noticed. The measurement was repeated five times and the observed values are shown in Figure 4.8.

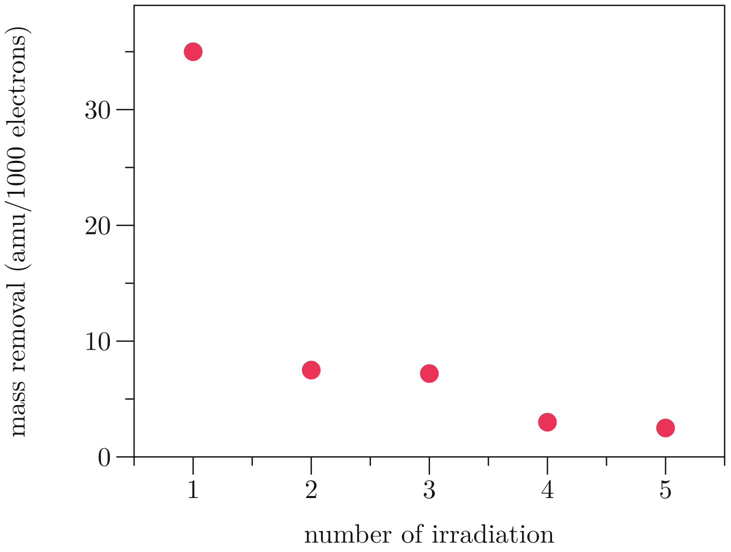

Figure 4.8: Detected mass removal under electron bombardment with an energy of 80 eV over the course of five different experiment runs. The observed mass ejection dropped from 35 amu/1000 electrons in the first measurement to 2.5 amu/1000 electrons in the fifth experiment.

In the first measurement, also visualized in Figure 4.6, a mass reduction of 35 amu/1000 electrons was detected. During the following two experiments the mass removal dropped to around 7.5 amu/1000 electrons. In the last two measurements values of around 2.5 amu/1000 electrons were detected.
In addition to these 80 eV experiments, the electron energy was further elevated to 150 eV and 300 eV and the corresponding mass ejection was measured. The obtained mass removal for all performed measurements with different electron energy is shown

in Figure 4.9.

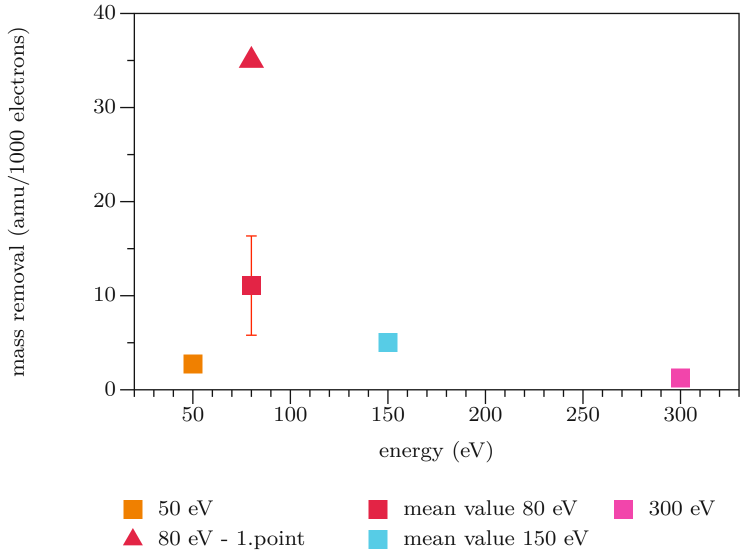

Figure 4.9: Measured mass removal under electron irradiation with electron energies up to 300 eV. The mass removal decrease with higher electron energy and at 300 eV a value of 1.24 amu/1000 electron is measured. The first measured 80 eV value (triangle) is listed separately.

For the 80 eV experiments, a mean value of 11.08 amu/1000 electrons is obtained. For further clarity the first 80 eV measurement point of around 35 amu/1000 electrons is also noted separately even though it is included in the mean value. After the 80 eV experiments were performed the energy was increased to 150 eV. During these measurements the detected mass removal is further reduced to a mean value of 5.03 amu/1000 electrons. In the last step the energy is elevated to 300 eV and the value for the mass removal per 1000 incident electrons decreased to 1.24 amu.
It seems that with additional measurements, the observed rate of mass removal steady decreases and the value from the first measurements could not be reproduced. As some studies also involve heating the LiF [40], the quartz was subsequently heated up to 120°C in an attempt to improve the reproducibility.

4.4.3 Heating of the LiF Sample

Since the values obtained for the mass removal at room temperature could not be reproduced in additional measurements, the LiF sample was heated to 120°C. This temperature was selected as it corresponds to the minimum of the resonance frequency of the quartz as a function of temperature. This temperature dependence has the form of a third order polynomial with the other extremum at room temperature [65]. At these two temperatures, the resonance frequency is therefore particularly stable against slight changes in temperature.

Also in this case, experiments with an electron energy of 80 eV, 150 eV and 300 eV were performed. The obtained curves are shown in Figure 4.10.

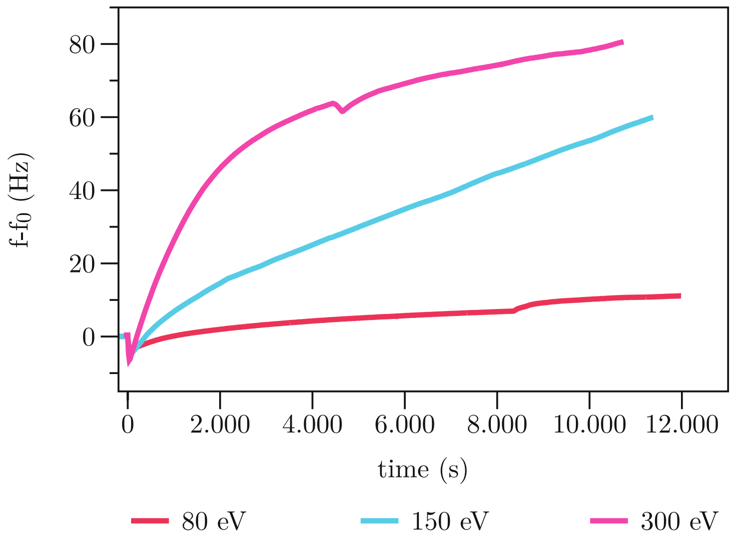

Figure 4.10: Recorded resonance frequency changes of the quartz at 120°C during electron irradiation of LiF with electron energies up to 300 eV. For all of the used electron energies an increase in the resonance frequency of the quartz is observed.

For all tested electron energies, a drop in the resonance frequency of around 6 Hz is observed in the first 100 s of the experiments, followed by an increase in the resonance frequency. For an electron energy of 80 eV, an increase in the quartz resonance frequency of around 15 Hz over the measurement time of 12000 s was observed. This increase in the resonance frequency is even more pronounced for higher electron energies of 150 eV with an increase of 65 Hz or at 300 eV with 85 Hz. For the 300 eV curve a decrease in the detected resonance frequency is visible at an irradiation time of about 4600 s. The decrease likely occurred due to temperature fluctuations, wherein the quartz – initially heated to 120°C – experienced a brief reduction of 2°C.

Again, the mass erosion was calculated in terms of mass removal per 1000 incoming electrons for the heated LiF sample (triangles). The results are illustrated in Figure 4.11. For a better comparison also the calculated values for the mass ejection at room temperature (rectangles) are shown.

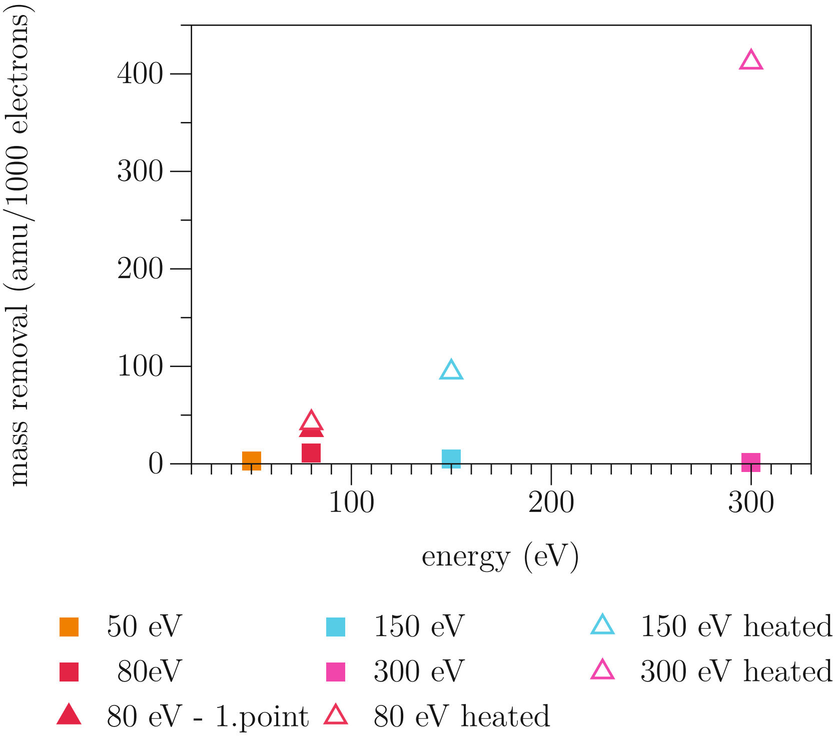

Figure 4.11: Mass erosion per 1000 incident electrons with an electron energy up to 300 eV for a LiF sample heated to 120°C (triangle). For comparison, also the values for the mass removal at room temperature (rectangles) for the same electron energies are given.

For the 80 eV measurement at 120°C, particularly with a number of 42 amu per 1000 electrons, only a slight variation from the first experiment conducted at room temperature with 80 eV is visible. Whereas the difference is more pronounced for the subsequent 80 eV measurements at room temperature with a mean mass removal of 11.08 amu/1000 electrons. By increasing the electron energy to 150 eV at 120°C quartz temperature, a mass removal of 94 amu/1000 electrons was observed. Further rising the electron energy to 300 eV leads to an increase to 412 amu/1000 electrons. At the final two electron energies of 150 eV and 300 eV, a distinct contrast between the measurements at room temperature and 120°C became evident.

4.5 Discussion of the Results

In this section, the previously presented data are discussed. At the beginning, the enstatite values are examined in more detail before the measured LiF data is compared with existing literature data.

In each conducted measurement, a minimum in the resonance frequency was observed within the first hundred seconds of irradiation. This decrease is particularly evident in Figure 4.3. The data presented suggest that with increasing energy of the incident electrons, a greater decrease in the resonance frequency of the individual measurements is observed. To get a deeper insight into this phenomenon, the power applied onto the quartz at different energies is considered. The corresponding power is estimated using the product of the applied electron current and the accelerating voltage. For $MgSiO_3$, the power input of the electron beam for each irradiation is calculated and illustrated in Figure 4.12. Moreover, Figure 4.12 also illustrates the variation in the detected minimum of the resonance frequency depending on the electron energy.

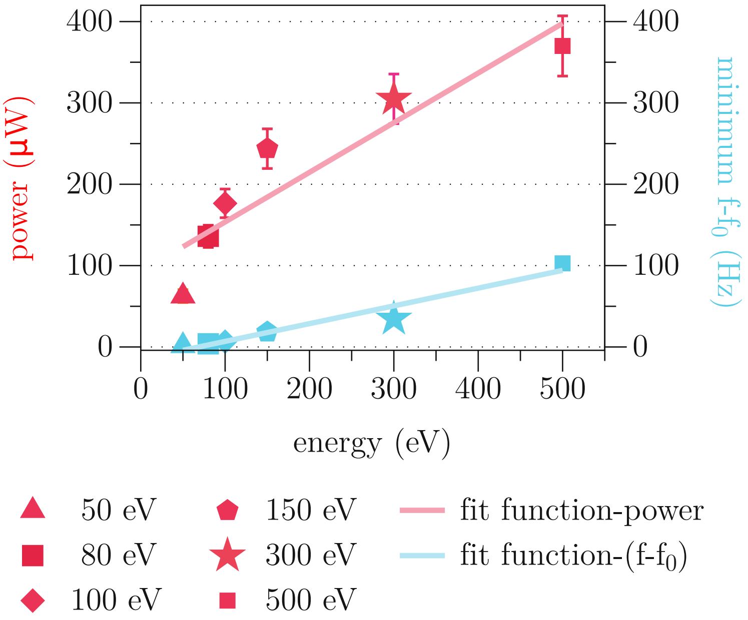

Figure 4.12: Detected minimum in the resonance frequency and power applied during the measurements with the $MgSiO_3$ sample for different electron energies up to 500 eV. With increasing electron energy, a nearly constant rise in power and the detected minimum is observed.

As the electron energy rises, the applied power increases steadily from 62 µW at 50 eV up to 372 µW at 500 eV. This suggests that with higher electron energies, the quartz is also exposed to an electron beam with higher power. The observed drop in resonance frequency at the start of each measurement (visualized, e.g, in Figure 4.3) can therefore be ascribed to a reaction of the QCM to the start of the electron irradiation: The QCM technique is highly sensitive to temperature, and when subjected to a sudden increase in power, this will lead to a local heating of the quartz. The heating then also scales with the power entry onto the QCM. Moreover, the observed frequency drops correspond to only small temperature differences [65]. These increases in temperature as inferred from the QCM resonance frequency are also in agreement with values obtained from a K type thermocouple, albeit mounted to the target holder next to the QCM rather than the quartz directly. Also, the lower minimum up to 104 Hz detected at higher energies, as shown in Figure 4.12 aligns with the corresponding increase in power at those energies. Furthermore, the minimum in the resonance frequency is also visible when using gold as a sample. In this case, no effect due to electron-stimulated desorption is expected [41], and any observed effects cannot stem from target films. This corroborates the claim that the detected minima in both experiments are inherent to the QCM technique itself and result from a temperature increase due to the incoming electron beam (power).

In addition, during the measurements with LiF a time resolved mass erosion was observed. In Figure 4.7, the mass removal decreased from 35 amu/1000 electron to 15 amu/1000 electrons. This reduction in mass erosion over the duration of the irradiation time was also seen in the other LiF experiments, indicated by the flattening of the gradient in the detected curves over the measurement time, as shown in Figure 4.6.

This phenomenon can be attributed to fluorine desorption and surface enrichment with lithium, as discussed in section 1.3 and 1.2.3 [46, 48]. The depletion of fluorine leads to less desorption of fluorine and a metallization of the surface, resulting in a decrease in mass removal.

A similar but less pronounced trend was observed during the $MgSiO_3$ experiments. In this scenario, the flattening can be attributed to both oxygen desorption and the depletion of oxygen on the surface [71, 72]. This depletion decreases the desorption of oxygen, consequently minimizing the mass erosion yield. The expected effect is comparable to what is seen by potential sputtering [73, 41].

Furthermore, the mass removal of the different samples Au, $MgSiO_3$ and LiF can be compared with each other. For this reason, the previously individually presented data of mass erosion are collectively compared in one graph in Figure 4.13 as the final result of this thesis. For a better overview, the y-axis has been scaled logarithmically and a linear fitting approach is applied to the data points for the LiF (blue curve) and the $MgSiO_3$ sample (orange curve). This further suggests that a linear correlation between the measured mass erosion and the electron energy for LiF and $MgSiO_3$ exists.

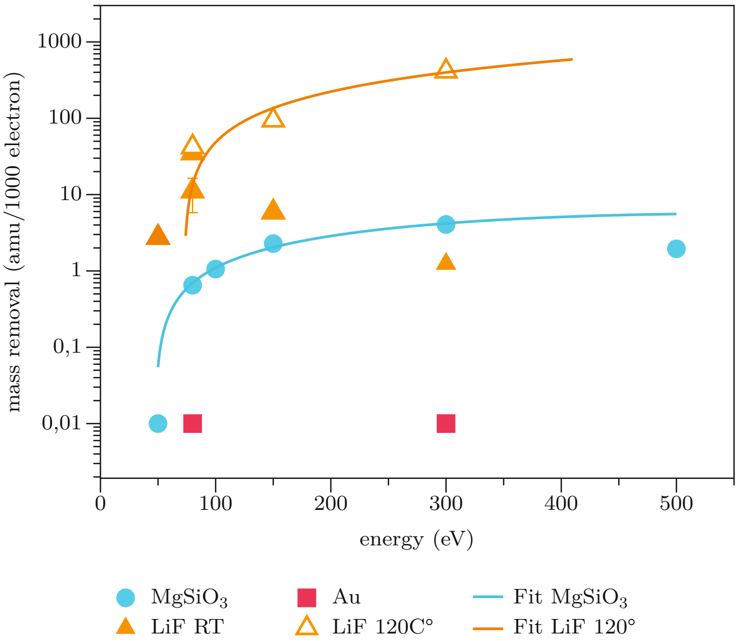

Figure 4.13: Comparison of the detected mass erosion for the MgSiO$_3$ (blue), LiF (orange) and the Au (red) sample. Furthermore, the LiF at 120°C and the MgSiO$_3$ values are fitted using linear regression of the data.

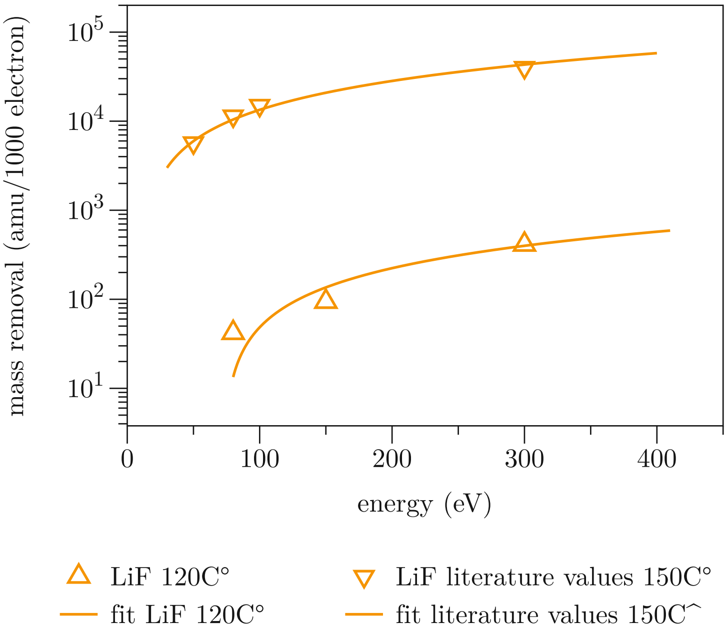

Figure 4.14: Comparison of the measured mass erosion for the LiF sample at 120C° and the literature values from Neidhart *et al.* at 150C° [40]. Both curves are fitted using a linaer regression of the data.

As mentioned in section 1.3, LiF has been extensively examined in the context of electron-stimulated desorption.

In this regard, the study by Neidhart *et al.* closely resembles the measurements conducted in this thesis [40]. This study examined the total sputter yield of LiF at a temperature of 150°C when exposed to electron irradiation ranging from 20 eV to 500 eV. Current densities of 20 nA/cm^2 were utilized, revealing a decline in the total sputter yield with increasing electron dose. This current density corresponds to a electron current of 160 pA in the FC utilized in this thesis and is therefore considerably lower than in our measurements. Figure 4.14 illustrates the measured total sputter yields for LiF by electrons as reported by Neidhart *et al* [40] in comparison to the values measured in this thesis at 120C°.

The literature-reported values of 5700 amu/1000 electrons at 50 eV electron energy and 11400 amu/1000 electrons at 80 eV are notably higher than the values presented in this study.

One possible explanation for this discrepancy could be the higher electron dose of around 1150 nA/cm^2 used in our experiments, since a decline in the yield with higher electron dose was observed by Neidhart *et al* [40]. The electron dose in this experiment is dictated by the utilized electron source and can only be minimally influenced. Another explanation may be that the decrease in the observed mass ejection with an increased number of experiment runs at room temperature, as shown in 4.4.2, may also be present at higher temperatures and therefore reduced values for the mass erosion were detected.

Figures 4.13 and 4.8 show the reduction in the mass ejection at room temperature by increasing electron energy and consequently electron dose and number of irradiations. This may be due to the Li enrichment at the surface [46] of the sample. It may also be the case that the sample becomes charged especially at room temperature, subsequently repelling the incoming negatively charged electrons. Another possibility emerges when examining Figure 4.5. Specifically for gold, there is a notable decrease of the resonance frequency at higher energies that persists well after the irradiation begins. This factor could also be considered at higher energies for different samples as it may lead to a reduction in the observed yield (positive slope of the resonance frequency) at these energies through superposition of the negative drift as seen in Figure 4.5. However, the linear correlation between the electron energy and the mass erosion for the LiF sample at 120°C detected in this thesis at least qualitatively corresponds to the findings of Neidhart *et al* [40].

Furthermore, the increase in the measured mass removal at elevated temperature compared to room temperature may also be explained with the theory described in chapter 1.2.3. The Li layer formed on the surface of the sample during irradiation may potentially evaporate and Li atoms desorb [41, 43]. Moreover, possible charging effects of the LiF sample occurring at room temperature are suppressed at higher temperature due to the start of ionic , which increases the measured mass erosion at 120°C.

The determined mass erosion for the enstatite sample was investigated for various energies up to 500 eV. These specific energies were selected because they are comparable to the energies of electrons in the solar wind. As described in section 1.1, the electrons can be categorized into four regimes depending on their energy. Although it was not feasible to achieve electron energies in the range of several keV with the utilized electron source *FS40A1*, which corresponds to the *super halo* population, energies up to 500 eV represent all other categories.

Furthermore, these higher energetic electrons are less present in the electron energy flux at lunar distances, as illustrated in Figure 11 in [74]. This graphic indicates that electrons with energies of over 10 keV are four orders of magnitude less frequent than those at approximately 100 eV. The Figure also indicates that electron energies of up to 500 eV makes up the major part of the electron energy distribution.

When comparing the $MgSiO_3$ mass erosion rate of 0.65 amu/1000 electrons with the LiF value at 120°C of 42 amu/1000 electrons at 80 eV, the rate for $MgSiO_3$ is approximately 1-2,% of that for LiF. The relatively low desorption observed for the enstatite sample persisted even at higher energies up to 300 eV. This difference was further highlighted by comparing the desorption rate of 4.06 amu/1000 electrons for the enstatite sample with the rate of 412 amu/1000 electrons for the LiF target.

The low desorption rate observed for the enstatite sample also agrees with the results of a study by McLain *et al.* [75]. In this research, various silicate samples were irradiated with an electron beam up to an energy of 500 eV, and the ejected particles were detected using a time-of-flight mass spectrometer and a quadrupole mass spectrometer. Throughout the study, no singly or doubly charged Mg ions were observed, which might explain the small desorption rate of $MgSiO_3$ observed in this study [75]. Furthermore, the absence of Mg reported in [75] could corroborate that any observed desorption could be driven primarily by the desorption of oxygen. Future experiments could investigate the desorption of sodium (Na) and calcium (Ca) using plagioclase samples, which also occur on the Moon and Mercury [76]. These measurements build on earlier findings of [75] which observed sodium erosion under electron bombardment with electron energies up to 150 eV.

When further comparing the mass removal on the enstatite sample due to electron bombardment with those from ions, with a sputter yield of 17.6 amu/ion [77], a clear difference of four orders of magnitude is observed. However, to accurately assess the impacts on the lunar surface, the electron and ion flux has to be taken into account as well. For the electron energies used in this study, a flux ranging from 10^6 to $10^8\,\mathrm{cm^{-2}s^{-1}}$ is anticipated. These values are similar to the expected ion fluxes for the utilized ion energies in [77]. With the similar flux for electrons and ions, the effect of electrons in the solar wind to erosion of the lunar and hermean surface is expected to be small as compared to the impact of ions in the solar wind.

5 Conclusion and Outlook

In the presented, work a suitable measurement procedure for electron-stimulated desorption measurements using a QCM was implemented. The aim was to investigate the contribution of the electrons as part of the solar wind in the formation of an exosphere around rocky bodies in space like the Moon or Mercury. Using a QCM enables real-time and *in-situ* observation of particle ejection caused by the desorption from thin films deposited on the quartz. Since this technique is very temperature sensitive, and the electron beam is generated through thermionic emission, the first aim was to minimize the perturbation to the QCM resonance frequency stability while switching the electron beam on and off. Therefore, the settings of the used electron source *FS40A1* and the effects on the generated electron beam have been examined in great detail. By adjusting the extractor voltage, the frequency experienced minimal impact, and additionally, it enabled the generation of a beam that remains stable and consistent over time.

Further, desorption measurements were conducted using the mineral enstatite $MgSiO_3$ that can serve as an analogue material for the pyroxene contribution in the lunar and hermean surface composition. In this context, irradiations with electron energies in the range from 10 eV-500 eV were executed. A net mass ejection was calculated for each experiment and a threshold energy around 80 eV was detected. Furthermore, a linear correlation between the measured mass erosion and the electron energy was observed.

Moreover, to validate the experiments with $MgSiO_3$, measurements were conducted using both a gold sample and a lithium fluoride sample as benchmarks. While the former should not exhibit electron stimulated desorption from a clean surface, the latter is known to have relatively high mass yields under electron bombardment. For LiF, experiments were performed at room temperature and at 120°C and a linear dependency between the electron energy and the observed mass erosion was found for the heated LiF sample. At room temperature, multiple measurements were rather inconclusive between measurement runs. Additional experiments will be necessary to provide a deeper insight into the observed steady decrease in the measured mass erosion at room temperature. While could be either due to charging of the sample or changes in surface composition due to preferential desorption.

This thesis encourages further experimental studies at elevated temperatures for the enstatite sample. In doing so, a deeper understanding of the impact of electrons in the solar wind on the formation of an exosphere around rocky bodies at different temperatures could be gained. In this case the minimum of the resonance frequency of the quartz as function of temperature is located at at around 120°C. This temperature is particularly advantageous here because it is comparable to the equatorial Moon surface temperature on the day side [78]. Furthermore, a rough evaluation was performed to estimate the significance of electrons in the solar wind to the mass ejection as compared to ions, comparing the measured values for the $MgSiO_2$ sample and the corresponding values for ion impact from [77]. Although this estimate suggests that electrons are responsible for only a small fraction (typically 1-2%) of the mass removal compared to ions, their significance is still noteworthy. Electrons play an important role in the desorption of adsorbed species [52, 51] and are likely involved in the formation of water on the lunar surface [79]. Also the interaction from electrons with water ice is well-documented through experimental research [80].

List of Figures

Bibliography

[1] G. Neukum et al. „Impact phenomena of micrometeorites on lunar surface material“. *Earth and Planetary Science Letters* 8 (1970), pp. 31–35.

[2] V. Griseri et al. „Space-Charge Detection and Behavior Analysis in Electron Irradiated Polymers“. *IEEE Transactions on Plasma Science* 34 (2006), pp. 2185–2190.

[3] C. Pieters and S. Noble. „Space weathering on airless bodies“. *Journal of Geophysical Research: Planets* 121 (2016), pp. 1865–1884.

[4] R. Herrick and N. Forsberg-Taylor. „The shape and appearance of craters formed by oblique impact on the Moon and Venus“. *Meteoritics & Planetary Science* 38 (2003), pp. 1551–1578.

[5] D. Janches et al. „Meteoroids as One of the Sources for Exosphere Formation on Airless Bodies in the Inner Solar System“. *Space Science Reviews* 217 (2021), p. 50.

[6] W. Cassidy and B. Hapke. „Effects of darkening processes on surfaces of airless bodies“. *Icarus* 25 (1975), pp. 371–383.

[7] C. Bennett, C. Pirim, and T. Orlando. „Space-Weathering of Solar System Bodies: A Laboratory Perspective“. *Chemical Reviews* 113.12 (2013), pp. 9086–9150.

[8] P. Wurz et al. „Self-consistent modelling of Mercury’s exosphere by sputtering, micro-meteorite impact and photon-stimulated desorption“. *Planetary and Space Science* 58 (2010), pp. 1599–1616.

[9] R. Vervack et al. „Mercury’s Complex Exosphere: Results from MESSENGER’s Third Flyby“. *Science* 329 (2010), pp. 672–675.

[10] *NASA - NSSDCA - Spacecraft - Details*. URL: `https://nssdc.gsfc.nasa.gov/nmc/spacecraft/display.action?id=2023-118A` (visited on 02/08/2024).

[11] *NASA-Website, Artemis mission*. URL: `https://www.nasa.gov/specials/artemis/index.html` (visited on 02/21/2024).

[12] S. Stern. „The lunar atmosphere: History, status, current problems, and context“. *Reviews of Geophysics* 37 (1999), pp. 453–491.

[13] A. Berezhnoi et al. „The surface of the Moon as a calibration source for Na and K observations of the lunar exosphere“. *Planetary and Space Science* 228 (2023), p. 105648.

[14] E. Leer, T. Holzer, and T. Flå. „Acceleration of the solar wind“. *Space Science Reviews* 33 (1982), pp. 161–200.

[15] G. Newkirk. „Structure of the Solar Corona“. *Annual Review of Atronomy and Astrophysics* 5 (1967), pp. 213–266.

[16] W. Feldman et al. „Solar wind electrons“. *Journal of Geophysical Research* 80 (1975), pp. 4181–4196.

[17] U. Feldman, E. Landi, and N. A. Schwadron. „On the sources of fast and slow solar wind“. *Journal of Geophysical Research: Space Physics* 110 (2005).

[18] L. Fisk, N. Schwadron, and T. Zurbuchen. „On the Slow Solar Wind“. *Space Science Reviews* 86 (1998), pp. 51–60.

[19] W. Axford. „The solar wind“. *Solar Physics* 100 (1985), pp. 575–586.

[20] P. Louarn et al. „On the Temporal Variability of the “Strahl” and Its Relationship with Solar Wind Characteristics: STEREO SWEA Observations“. *Solar Physics* 259.1 (2009), pp. 311–321.

[21] P. Szabo et al. „Experimental Insights Into Space Weathering of Phobos: Laboratory Investigation of Sputtering by Atomic and Molecular Planetary Ions“. *Journal of Geophysical Research: Planets* 125 (2020).

[22] H. Biber et al. „Solar wind Helium ion interaction with Mg and Fe rich pyroxene as Mercury surface analogue“. *Nuclear Instruments and Methods in Physics Research Section B: Beam Interactions with Materials and Atoms* 480 (2020), pp. 10–15.

[23] M. Schaible et al. „Solar Wind Sputtering Rates of Small Bodies and Ion Mass Spectrometry Detection of Secondary Ions“. *Journal of Geophysical Research: Planets* 122 (2017), pp. 1968–1983.

[24] M. Schaible and R. Baragiola. „Hydrogen implantation in silicates: The role of solar wind in SiOH bond formation on the surfaces of airless bodies in space“. *Journal of Geophysical Research: Planets* 119 (2014), pp. 2017–2028.

[25] A. Milillo et al. „Future Directions for the Investigation of Surface-Bounded Exospheres in the Inner Solar System“. *Space Science Reviews* 219 (2023), p. 49.

[26] V. Ageev. „Desorption induced by electronic transitions“. *Progress in Surface Science* 47 (1994), pp. 55–203.

[27] B. Yakshinskiy and T. Madey. „Photon-stimulated desorption of Na from a lunar sample: temperature-dependent effects“. *Icarus* 168 (2004), pp. 53–59.

[28] D. Menzel. „Electron stimulated desorption: Principles and recent developments“. *Surface Science* 47 (1975), pp. 370–383.

[29] G. Hayderer et al. „A highly sensitive quartz-crystal microbalance for sputtering investigations in slow ion–surface collisions“. *Review of Scientific Instruments* 70 (1999), pp. 3696–3700.

[30] P. Szabo et al. „Solar wind sputtering of wollastonite as a lunar analogue material – Comparisons between experiments and simulations“. *Icarus* 314 (2018), pp. 98–105.

[31] H. Biber et al. „Sputtering Behavior of Rough, Polycrystalline Mercury Analogs“. *The Planetary Science Journal* 3 (2022), p. 271.

[32] D. Menzel and R. Gomer. „Electron-Impact Desorption of Carbon Monoxide from Tungsten“. *The Journal of Chemical Physics* 41 (1964), pp. 3329–3351.

[33] P. Redhead. „Interaction of slow electrons with chemisorbed oxygen“. *Canadian Journal of Physics* 42 (1964), pp. 886–905.

[34] M. Knotek. „Stimulated desorption“. *Reports on Progress in Physics* 47 (1984), pp. 1499–1561.

[35] H. Mustrop and S. Ernst. „Das Franck-Condon-Prinzip“. *Chemie in unserer Zeit* 4 (2011), pp. 256–269.

[36] D. Menzel and R. Gomer. „Desorption from Metal Surfaces by Low-Energy Electrons“. *The Journal of Chemical Physics* 41 (1964), pp. 3311–3328.

[37] R. Ramsier and J. Yates. „Electron-stimulated desorption: Principles and applications“. *Surface Science Reports* 12 (1991), pp. 246–378.

[38] P. Feibelman and M. Knotek. „Reinterpretation of electron-stimulated desorption data from chemisorption systems“. *Physical Review B* 18 (1978), pp. 6531–6539.

[39] L. Markowski and F. Gołek. „ESD from LiF thin films“. *Surface Science* 394 (1997), pp. 144–149.

[40] T Neidhart et al. „Determination of electron-induced total sputter yield of LiF“. *Nuclear Instruments and Methods in Physics Research Section B: Beam Interactions with Materials and Atoms*. Desorption Induced by 101 (1995), pp. 127–130.

[41] F. Aumayr and H. Winter. „Potential sputtering“. *Philosophical Transactions of the Royal Society of London. Series A: Mathematical, Physical and Engineering Sciences* 362 (2004), pp. 77–102.

[42] M. Draxler et al. „Apparent Velocity Threshold in the Electronic Stopping of Slow Hydrogen Ions in LiF“. *Physical Review Letters* 95.11 (2005), p. 113201.

[43] R. Williams and K. Song. „The self-trapped exciton“. *Journal of Physics and Chemistry of Solids* 51.7 (1990), pp. 679–716.

[44] R. T. Williams et al. „Off-center self-trapped excitons and creation of lattice defects in alkali halide crystals“. *Physical Review B* 33.10 (1986), pp. 7232–7240.

[45] M. Piacentini. „A new interpretation of the fundamental exciton region in LiF“. *Solid State Communications* 17.6 (1975), pp. 697–700.

[46] J. Kelber and K. Bieg. „Surface analysis of LiF films by electron stimulated desorption and x-ray photoelectron spectroscopy“. *Applied Surface Science* 27 (1986), pp. 151–163.

[47] J. Sarnthein et al. „Electron-stimulated desorption of lithium from LiF and the influence of metal islands on the surface“. *Surface Science* 241 (1991), pp. 6–10.

[48] F. Gołek and W. Sobolewski. „Thresholds of ESD for LiF thin layers“. *Vacuum* 63 (2001), pp. 3–6.

[49] B. Yakshinskiy and T. Madey. „Photon-stimulated desorption as a substantial source of sodium in the lunar atmosphere“. *Nature* 400.6745 (1999), pp. 642–644.

[50] B. Yakshinskiy and T. Madey. „DIET of alkali atoms from mineral surfaces“. *Surface Science* 528.1 (2003), pp. 54–59.

[51] B. Yakshinskiy and T. Madey. „Temperature-dependent DIET of alkalis from SiO2 films: Comparison with a lunar sample“. *Surface Science* 593.1 (2005), pp. 202–209.

[52] T. Madey et al. „Desorption of alkali atoms and ions from oxide surfaces: Relevance to origins of Na and K in atmospheres of Mercury and the Moon“. *Journal of Geophysical Research: Planets* 103 (1998), pp. 5873–5887.

[53] R. Killen et al. „An Estimate of the Importance of Electron Sputtering at Mercury“. 55 (2023), p. 116.03.

[54] D. Mattox. „Particle bombardment effects on thin-film deposition: A review“. *Journal of Vacuum Science & Technology A: Vacuum, Surfaces, and Films* 7 (1989), pp. 1105–1114.

[55] P. Sigmund. „Sputtering by ion bombardment theoretical concepts“. *Sputtering by Particle Bombardment I: Physical Sputtering of Single-Element Solids.* Berlin, Heidelberg, 1981, pp. 9–71.

[56] W. Eckstein et al. „Threshold energy for sputtering and its dependence on angle of incidence“. *Nuclear Instruments and Methods in Physics Research Section B: Beam Interactions with Materials and Atoms* 83 (1993), pp. 95–109.

[57] P. Sigmund. „Theory of Sputtering. I. Sputtering Yield of Amorphous and Polycrystalline Targets“. *Physical Review* 184 (1969), pp. 383–416.

[58] J. Malherbe, S. Hofmann, and J. Sanz. „Preferential sputtering of oxides: A comparison of model predictions with experimental data“. *Applied Surface Science* 27 (1986), pp. 355–365.

[59] R. Wilhelm. „Ion beam analysis: fundamentals and applications“. Lecture Notes. TU Wien, 2023.

[60] J. Kistemaker and H. Roosendaal. „Fundamental Processes in Surface Erosion by Sputtering“. *Japanese Journal of Applied Physics* 13 (1974), p. 571.

[61] P. Kelly and R. Arnell. „Magnetron sputtering: a review of recent developments and applications“. *Vacuum* 56 (2000), pp. 159–172.

[62] J. Thornton. „Magnetron sputtering: basic physics and application to cylindrical magnetrons“. *Journal of Vacuum Science and Technology* 15 (1978), pp. 171–177.

[63] A. Golczewski et al. „A quartz-crystal-microbalance technique to investigate ion-induced erosion of fusion relevant surfaces“. *Nuclear Instruments and Methods in Physics Research Section B: Beam Interactions with Materials and Atoms* 267 (2009), pp. 695–699.

[64] G. Sauerbrey. „Verwendung von Schwingquarzen zur Wägung dünner Schichten und zur Mikrowägung“. *Zeitschrift für Physik* 155 (1959), pp. 206–222.

[65] R. Stadlmayr et al. „A high temperature dual-mode quartz crystal microbalance technique for erosion and thermal desorption spectroscopy measurements“. *Review of Scientific Instruments* 91 (2020), p. 125104.

[66] D. Pierce, K. Yoonkee, and J. Vig. „A temperature insensitive quartz microbalance“. *IEEE Transactions on Ultrasonics, Ferroelectrics and Frequency Control* 45 (1998), pp. 1238–1245.

[67] E. Galutschek et al. „Compact 14.5 GHz all-permanent magnet ECRIS for experiments with slow multicharged ions“. *Journal of Physics: Conference Series* 58.1 (2007), p. 395.

[68] R. Stadlmayr et al. „Sputtering of nanostructured tungsten and comparison to modelling with TRI3DYN“. *Journal of Nuclear Materials* 532 (2020), p. 152019.

[69] G. Hayderer. „Projectile charge state dependent sputtering of solid surfaces“. PhD thesis. TU Wien, 2000.

[70] H. Biber. „Sputtering investigations of wollastonite using solar wind ions“. Master thesis. TU Wien, 2018.

[71] H. Hijazi et al. „Kinetic and potential sputtering of an anorthite-like glassy thin film“. *Journal of Geophysical Research: Planets* 122.7 (2017), pp. 1597–1609.

[72] A. Barghouty et al. „Solar-wind protons and heavy ions sputtering of lunar surface materials“. *Nuclear Instruments and Methods in Physics Research Section B: Beam Interactions with Materials and Atoms* 269.11 (2011), pp. 1310–1315.

[73] P. Szabo et al. „Dynamic Potential Sputtering of Lunar Analog Material by Solar Wind Ions“. *The Astrophysical Journal* 891 (2020), p. 100.

[74] P. Wurz et al. „Particles and Photons as Drivers for Particle Release from the Surfaces of the Moon and Mercury“. *Space Science Reviews* 218 (2022), p. 10.

[75] J. McLain et al. „Electron-stimulated desorption of silicates: A potential source for ions in Mercury’s space environment“. *Journal of Geophysical Research* 116 (2011).

[76] A. Jull et al. „Sputtering rates of minerals and implications for abundances of solar elements in lunar samples“. *Nuclear Instruments and Methods* 168.1 (1980), pp. 357–365.

[77] H. Biber. „Influence of ion sputtering on the surfaces of Mercury and the Moon“. PhD thesis. Technische Universität Wien, 2023.

[78] J. Williams et al. „The global surface temperatures of the Moon as measured by the Diviner Lunar Radiometer Experiment“. *Icarus* 283 (2017), pp. 300–325.

[79] S. Li et al. „Formation of lunar surface water associated with high-energy electrons in Earth's magnetotail“. *Nature Astronomy* 7.12 (2023), pp. 1427–1435.

[80] A. Galli et al. „0.2 to 10 keV electrons interacting with water ice: Radiolysis, sputtering, and sublimation“. *Planetary and Space Science* 155 (2018), pp. 91–98.

Danksagung

Zum Abschluss möchte ich die Gelegenheit nutzen und mich bei allen bedanken, die mich beim Erstellen dieser Arbeit begleitet und unterstützt haben. .

Lieber Fritz, gleich zu Beginn möchte ich mich bei dir bedanken, dass du nach meine Bachelorarbeit nun auch meine Diplomarbeit betreut hast. Durch deine offene und herzliche Art wird das ganze Klima der Arbeitsgruppe positiv beeinflusst. Auch mit deinen Vorschlägen und Ideen eröffnest du öftmals eine neue Perspektive auf so manches Problem.

Ein herzlichen Dank auch dir lieber Johannes. Du hast mir nicht nur mit deinem technischen Know-how viel Wissen vermittelt sondern auch abseits von der Physik. Mit deinem breiten Kentnissen im Bereich von Tee über Minaeralien bis hin zum Brot backen, war ich auch in diesen Gebieten immer wieder erstaunt von deinem Wissen. Neben der zuverlässigen Versorgung der ganzen Gruppe mit Kaffee, sorgst du auch als persönlicher Yoja-Coach abseits von dem vielleicht stressigen Laboralltag für lustige Momente.

Auch bei den restlichen Mitgliedern der Arbeitsgruppe möchte ich mich herzlich bedanken. Zunächst an meine lieben Kollegen aus dem SSpassssBüro, Lidija, Martina, Benji, Johannes (und Geroge), mit euren Katzenkalender, der persönlichen Spotify-playlist und den äuserst produktivenÜnterhaltungen macht ihr euch jeden Tag ein bisschen spassiger. Danke, dass ihr mich so herzlich aufgenommen habt. Aber auch ein herzliches Dankeschön an den Rest der Gruppe; Anna, Matthias, Daniel, Alex, Markus, Florian, Felix, Fil, Vicky und Richard für die vielen lustigen Kaffee-/Teepausen mit Kreuzworträtseln, Katzen und allerlei lustigen und interessanten Diskussionen rund um fast jedes denkbare Thema. Weiters möchte ich mich bei meinen Studienkollegen und Freunden bedanken, die mich teilweise seit dem ersten Semester begleiten. Vorallem mein Laborbuddy"Viola; seit der ersten Grundlagen-Übung, hast du es geschafft jede Vorlesung etwas lustiger zu machen.

Zum Schluss möchte ich mich bei meinen Eltern, meiner Schwester und Daisy für eure konsequente positive Ermutigung, teilweise auch ohne Worte, bedanken.